Journal Name

ARTICLE TYPE

Cite this: DOI: 00.0000/xxxxxxxxxx

Organic Electrochemical Transistors - From Device Models to a Targeted Design of Materials

Pushpa Raj Paudel,[a] Joshua Tropp,[b] Vikash Kaphle,[a,b] Jason David Azoulay,[b] and Björn Lüssem*[a]

Received Date
Accepted Date

DOI: 00.0000/xxxxxxxxxx

Organic electrochemical transistors (OECTs) are highly versatile in terms of their form factor, their fabrication technology, and their freedom in the choice of substrate material. Their ability to transduce ionic into electric signals and the use of bio-compatible organic materials makes them ideally suited for a wide range of applications, in particular in areas where electronic circuits are interfaced with biologic matter. OECT technology has attracted widespread interest during the last years, which was accompanied with a steady increase in its performance. However, this progress was mainly driven by optimization and less by a targeted design of new device geometries and OECT materials. To narrow this gap, this review provides an overview on the different device models used to explain the underlying physics governing the steady and transient behavior of OECTs. It is shown how the models can be used to find synthetic targets for better performing OECT materials and various materials classes used for OECTs are summarized. Overall, a road-map of future research in new device models and material design is presented summarizing the most pressing open questions in the understanding of OECTs.

1 Introduction

A continuous decrease in production cost alongside an ever increasing performance has made transistors ubiquitous in our daily life. Whereas crystalline silicon is used in high-speed complementary metal-oxide semiconductor (CMOS) circuits, a wide variety of materials such as oxide semiconductors, polycrystalline silicon, or even organic semiconductors is used for thin film transistors (TFTs).

In recent years transistors have moved into the focus of research that can be interfaced with biological systems. For these applications, signals carried by ion currents have to be transduced into electric ones. Thus, a new transistor technology based on semiconducting materials that can conduct both, ionic and electronic charge, became of crucial importance:[1] Organic Electrochemical Transistors (OECTs).[2]

Organic electrochemical transistors are highly versatile in terms of device design, fabrication technology and choice of substrates. The use of organic semiconducting polymers as channel material opens the possibility for low-cost processing technologies such as screen-printing,[3–5] spray-coating,[6] inkjet printing,[7,8] or inexpensive 3D printing like fused deposition modeling (FDM).[9] OECTs have been processed on rigid glass substrates,[10] flexible plastic substrates,[11–13] on paper,[13,14] textiles,[15] fabric,[16,17] carbon nanotubes fibers,[18] ultra-thin films like parylene,[6] and onto stretchable substrates.[19,20] In addition to the stretchable nature of some OECTs[21] some of the semiconductors used are self-healable[22,23], making them ideal candidates for implantable electronics. Some OECTs have a planar geometry,[24,25] i.e. all three terminal are in a single plane, whereas others are vertical[5,26] with the gate in a different plane as the source and drain contact. OECTs have been integrated with microfluidic circuits[27–29] while some have channels in the form of 3D scaffolds.[30,31]

Not only are OECTs highly versatile in terms of their shape and form factor, but can as well be optimized for various applications. OECTs are e.g. used as bio-chemical sensors,[28,28,29,32–39] electrophysiological sensors,[18,40,41] neuromorphic devices,[9,42–44] pressure sensors,[45] or wearable[15–17] and implantable devices.[18,46,47] Their stability was also found to be satisfactory for their intended use.[23,24,48]

The general setup of an Organic Electrochemical Transistor (OECT) is shown in Figure 1. Similar to the other transistor technologies, OECTs have three terminals labeled Source (S), Drain (D) and Gate (G). The source and drain electrode are in contact with a thin film of an organic semiconducting layer forming the transistor channel.

The transistor channel is connected to the gate electrode by an electrolyte. The distribution of ions inside the electrolyte and

[a] Department of Physics, Kent State University, Kent, Ohio 44240, USA. Fax: 330-672-2959; Tel: 330-672-2246; *E-mail: blussem@kent.edu
[b] School of Polymer Science and Engineering, The University of Southern Mississippi, Hattiesburg, MS 39406, USA.

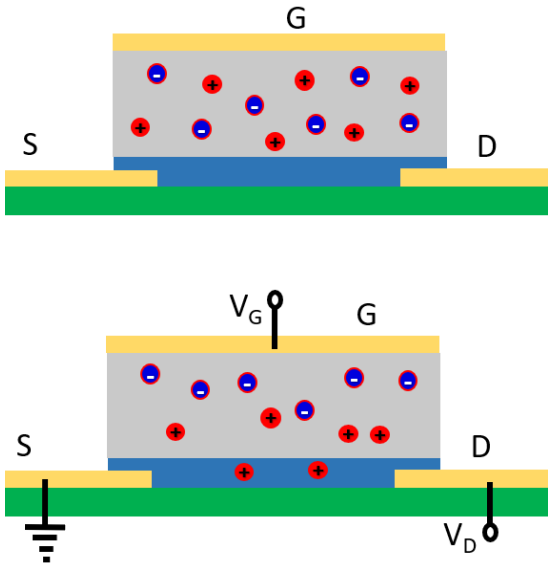

Fig. 1 Schematic diagrams of an Organic Electrochemical Transistor (OECT) and its operation mechanism.

semiconductor channel can be controlled by the potential applied to the gate $V_G (\equiv V_{GS})$. In Figure 1, a positive voltage is applied to the gate electrode, which forces cations to move into the semiconductor channel.[49] Inside the channel, these ions can dope or de-dope the semiconductor, which changes the charge carrier concentration inside the transistor channel. Hence, the conductivity of the semiconductor and the magnitude of the drain current is modulated by the amount of injected ions and thus the gate voltage.[50]

There are two different operation modes, depending on the way the charge carrier density is modulated: depletion and accumulation mode.[51] In OECTs operating in the depletion mode, the semiconductor material is electrically doped, resulting in a large density of free charge carries and therefore a high conductivity even without an applied gate voltage. Forcing ions into the semiconductor leads to a de-doping of the bulk of the channel, which in turn results in a decrease of the charge carrier density, the channel conductivity, and hence the drain current. If the gate potential is sufficiently large, the drain current can be completely suppressed and the transistor is switched off.

In comparison to depletion type OECTs, OECTs operating in accumulation mode are initially devoid of charge carriers and the transistor is in its off-state. Applying a gate potential V_G will again force ions into the transistor channel, which however are designed to dope the material and to increase its conductivity.

Several semiconducting materials were developed for OECTs. The most commonly used material is the p-doped semiconductor poly(3,4-ethylenedioxythiophene) doped with poly(styrene sulfonate) (PEDOT:PSS).[52] Similarly, the polymer poly(2-(3,3-bis(2-(2-(2-methoxyethoxy)ethoxy)ethoxy)-[2,2'-bithiophen]-5-yl)thieno[3,2-b]thiophene), p(g2T-TT),[53] can be used as accumulation mode materials in which the presence of anions results in p-doping to switch the transistors into the ON state. Further materials classes were developed, but the field is slowed by an incomplete understanding of the details of OECTs operation mechanism and a lack in clear design rules for highly-efficient OECT materials.

To address this challenge, we intend to complement previous reviews on OECTs[54–58] and to bridge the gap between current device models and materials synthesis, hopefully stimulating a more targeted design of high-performance materials. To accomplish this aim, the most common OECT device models are reviewed here. An emphasis will be put on capacitive models[51,59,60](Section 2), before more refined models based on two-dimensional drift-diffusion simulations are discussed in Section 3). With the background in operation mechanisms of OECTs, recent developments in materials synthesis and novel OECT materials are summarized in Sections 5.1.1 to 5.1.5.

2 Compact Device Models Based on Capacitive Gate Coupling

2.1 Benards-Malliaras Model: Steady State Behaviour.

Although other device models were proposed before,[61,62] the device model proposed by D. A. Bernards and G. G. Malliaras in 2007[51] became the first standard model. Initially formulated for PEDOT:PSS based depletion OECTs, it is nowadays widely used to extract device and material parameters of a wide range of different OECTs.

The model of Bernards heavily relies on standard thin-film transistor theory and implicitly invokes the gradual channel approximation[63] of TFT theory. The device model is sketched in Figure 2. The transistor channel is assumed to have a length of L, a width of W, and a thickness of T. In the following, the x-axis extends from the edge of the source electrode at $x = 0$ to the edge of the drain electrode at $x = L$.

This complex three terminal OECT structure is separated into two independent parts - an electronic and an ionic circuit as shown in Figure 2. Transport of ionic charge in the electrolyte and the semiconductor is described by a series connection of an ionic resistance and a capacitive element resembling the gate capacitance used in standard thin-film transistors. The capacitance C_G is defined as the ratio of the charge of the injected ions per unit area $\frac{dQ(x)}{Wdx}$ to the voltage across the capacitor. If the current in the electrolyte is small, one obtains

$$C_G = \frac{dQ(x)}{dxW} \frac{1}{V_G - \phi(x)}, \tag{1}$$

with V_G the potential of the gate, and $\phi(x)$ the potential along the transistor channel.

Equation 1 assumes that without voltage applied across the gate capacitance, no cations are injected into the semiconductor. However, this assumption neglects any difference in the chemical potential at the gate and the source electrode, and furthermore any charge accumulation at the interface between the semiconductor and the electrolyte. To account for these effects, a threshold voltage V_T, neglected in original model of Bernards and Malliaras, can be defined similar to the threshold voltage of field effect transistors (FET). Thus, the charge dQ of cations injected

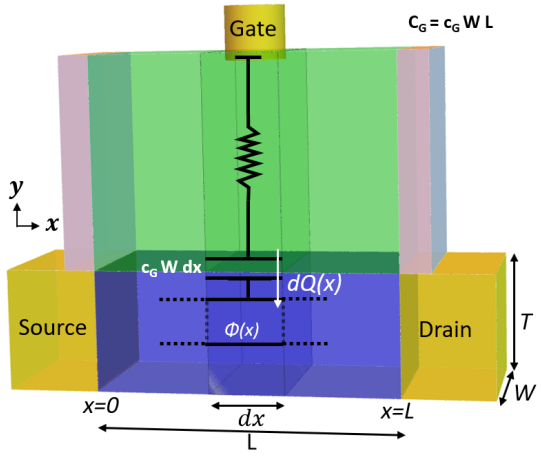

Fig. 2 OECT device geometry used in the Benards-Malliaras model. The channel is formed by an organic semiconductor of length L between source ($x=0$) and drain ($x=L$). A thin element of the channel (length dx, width W) at position x is sketched as well. Due to the voltage difference between the gate electrode and the channel potential $\phi(x)$, cations with a total charge $dQ(x)$ are injected into the channel.[51]

at x becomes:

$$dQ(x) = C_G \cdot W \cdot dx\ (V_G - V_T - \phi(x)), \tag{2}$$

and the total charge of cations that enter the transistor channel becomes:

$$Q = \int_0^L dQ(x)\ dx = C_G \cdot W \int_0^L (V_G - V_T - \phi(x))\ dx \tag{3}$$

The electronic part of the OECT is described by Ohm's law. Assuming a p-type semiconductor, one obtains

$$J(x) = -e\mu p(x)\frac{d\phi(x)}{dx} \tag{4}$$

where J is the current density, e is elementary charge, μ is the hole mobility, and $p(x)$ is the hole density along the channel.

The ionic and electronic systems of an OECT are strongly coupled. Bernards and Malliaras assumed the coupling to be mediated by an electrostatic de-doping process. Whenever the gate is positive with respect to the channel (i.e. $V_G > V_T + \phi(x)$), cations will migrate into the polymer. Assuming that the semiconductor remains electrically neutral, a hole will be extracted at the electrodes. Hence, assuming that every cation replaces one free hole, the hole concentration $p(x)$ along the transistor channel becomes:

$$p(x) = p_o\left(1 - \frac{dQ(x)}{ep_oWdxT}\right) \tag{5}$$

where p_o is the initial doping concentration inside the organic semiconductor.

Replacing the hole concentration in Equation 4 by Equation 5 and Equation 2 results in the steady state current density $J(x)$:

$$J(x) = e\mu p_o\left[1 - \frac{V_G - V_T - \phi(x)}{V_P}\right]\frac{d\phi(x)}{dx} \tag{6}$$

where $V_P = ep_oT/C_G$ is the pinch-off voltage of the transistor, which is a function of the device material, device geometry and doping concentration.

As the current density $J(x)$ has to be constant along the transistor channel, one can integrate Equation 6 to obtain an analytical expression for the drain current:

$$I_D = G\left[1 - \frac{V_G - V_T - \frac{V_D}{2}}{V_P}\right]V_D \tag{7}$$

where $G = e\mu p_o\frac{WT}{L}$ is the conductance of the channel without gate voltage applied.

This relation is valid for the linear regime of the transistor only, i.e. the region where no part of the channel is fully depleted of holes (i.e. for $V_D > V_G - V_T - V_P$). If the drain potential becomes too negative, i.e. for the region of $V_D < V_G - V_T - V_P$, the transistor channel is pinched off at the drain and the hole concentration drops to zero at the drain forming a highly resistive region. The drain current saturates and one obtains:

$$I_D = -G\frac{[V_G - V_T - V_P]^2}{2V_P} = -G\frac{[V_D^{sat}]^2}{2V_P} = -\mu C_G\frac{W}{2L}[V_D^{sat}]^2 \tag{8}$$

which is identified as saturation regime, where $V_D^{sat} = V_G - V_T - V_P$ is the drain voltage corresponding to V_G that marks the transition between saturation and linear regime.

Originally,[51] it was postulated that the total capacitance C_G scales with the device area, but it was shown later by Rivnay et al.[60] that C_G is proportional to the total volume of the semiconductor (cf. Figure 3). Similarly, Prigodin et al.[64] proposed in 2008 that the capacitance of a mixed conductor depends on its volume. Assuming that ions and electric charge are transported in the same phase, they were able to relate the capacitance to the screening length of ions and electrons/holes r_i and r_e at the interfaces to the mixed conductor

$$C_G = \frac{\varepsilon\varepsilon_0}{r_i^2 + r_e^2} \tag{9}$$

Scaling of the gate capacitance with the sample volume sets OECTs apart from other transistor technologies, i.e. it shows that charge is transported throughout the bulk of the semiconductor and not only at the dielectric/semiconductor interface. This property partially explains the high transconductance values observed in OECTs and hence their large signal amplification. Furthermore, the large gate capacitance justifies that charge accumulated in the double layers at the gate/electrolyte or electrolyte/semiconductor interfaces are often neglected. However, in particular for the use of OECTs as sensors, the fraction of the gate potential that drops across these interfaces and the double layer gate capacitances is essential, which is discussed more in detail in Section 5.2.

The assumption of a constant hole mobility neglects the fact that the transport in organic semiconductor is marked by hopping in a complex density of states, which is known to introduce a charge carrier dependency of the mobility.[65–68] Assuming an exponential density of states DOS, Friedlein et al.[59] were able to introduce a more complex mobility to the original Bernards-Malliaras model. Based on the work of Vissenberg et al.[68] they

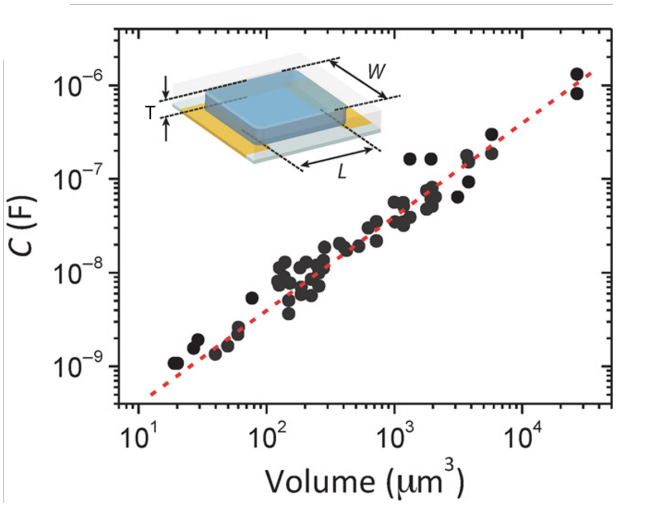

Fig. 3 PEDOT:PSS capacitance determined from impedance spectroscopy for devices of varying geometry. Inset: OECT configuration and channel dimensions (W, L, and T). The linear fit to the capacitance data (red dotted line) yields a volumetric capacitance $C^* = 39.3 \pm 1.3\ F\ cm^{-3}$. Adapted from AAAS with permission.[60] Copyright © 2015 Rivnay et al.

used the following dependence of charge carrier (hole) mobility on carrier density for disordered amorphous channel:

$$\mu(p) = \mu_o \left(\frac{p}{p_o}\right)^{\frac{E_o}{K_B\theta}-1} \tag{10}$$

where E_o is the disorder parameter describing the energetic width of the tail of the density of states, K_B is Boltzmann's constant, θ is temperature, and μ_o is a mobility prefactor that is independent of carrier concentration, but may depend on other factors such as temperature.

Using Equation 10, relation 7 becomes:

$$I_D = G\frac{1}{\frac{E_o}{K_B\theta}+1}V_P\left[\left(1-\frac{V_G-V_T-\frac{V_D}{2}}{V_P}\right)^{\frac{E_o}{K_B\theta}+1} - \left(1-\frac{V_G-V_T}{V_P}\right)^{\frac{E_o}{K_B\theta}+1}\right]V_D \tag{11}$$

for $V_D > V_G - V_T - V_P$ i.e. linear regime. The saturation current becomes (cf. Equation 8)

$$I_D = G\frac{1}{\frac{E_o}{K_B\theta}+1}V_P\left(1-\frac{V_G-V_T}{V_P}\right)^{\frac{E_o}{K_B\theta}+1} \tag{12}$$

Although the incorporation of a concentration dependent mobility is found to improve the fit of accumulation and depletion mode transistors[59,69] and seems to lead to an improved fit of the charge carrier distribution along the transistor channel,[59] the experimental results of Campbell et al.[70] indicate that - at least for some materials characterized in a standard OFET geometry - a dependency of carrier mobility on concentration can be absent or at least minimal.

Overall, the Bernard-Malliaras model has been proven useful for its simplicity and is often used to extract device parameters and to fit device characteristics. Not only is it used to discuss the steady-state of OECTs, but has been extended by several authors to describe the transient response of OECTs as well.

2.2 Benards-Malliaras Model: Transient Behavior of OECTs.

The first attempt to model transient behavior of OECTs was reported in the original Bernards-Malliaras model.[51] As already discussed for the steady-state model, the transient behavior of OECTs is determined by two systems - an electronic and an ionic one. The ionic contribution to the transient response $j_{ion}(x)$ is defined by injection of cations from the electrolyte into the organic film. The increase in net charge inside the organic film will be compensated by a removal of holes at the drain electrode. Hence, one obtains for the ion current as a function of position along the channel $j_{ion}(x,t)$

$$j_{ion}(x,t) = -e\frac{dp(x,t)}{dt}dx \tag{13}$$

Bernards and Malliaras simplified the problem by neglecting the the spatial variation of the potential and hole density along the channel, i.e. by using an average hole density $\overline{p}(t)$ and ionic current $\overline{j_{ion}}(t)$ only.

$$\overline{p}(t) = \frac{1}{L}\int_0^L dx\ p(x,t), \tag{14}$$

$$\overline{j_{ion}}(t) = \frac{1}{L}\int_0^L dx\ j(x,t) \tag{15}$$

Although the ionic gate current is assumed to be zero at steady state conditions, it is non-zero under transient conditions as ions move in and out of the organic layer, comparable to charging and discharging of a capacitor. Adding these time varying contributions, the drain current as a function of time can be approximated by:

$$J(t) = j_p(t) - \overline{j_{ion}}(t) = e\mu\overline{p}(t)\frac{V_D}{L} + efL\frac{d\overline{p}(t)}{dt} \tag{16}$$

where f is a proportionality factor that was introduced to account for the error made when neglecting the spatial variation of the doping and de-doping process and the ion current. This factor f is expected to depend on the gate and drain voltages.

Using Equation 5, the transient current $I(t) = J(t)\cdot W\cdot T$ as described by Equation 16 becomes

$$I(t) = G\left(1-\frac{Q(t)}{ep_o\mathbf{V}}\right)V_D - f\frac{dQ(t)}{dt} \tag{17}$$

where, $\mathbf{V} = WTL$ is the volume of the channel, T is the thickness of the channel and $Q(t)$ is the transient response of the relevant ionic circuit.

This general relation can be solved for two limiting cases, either assuming a constant gate current $I_G = \frac{dQ}{dt} = \frac{Q}{t}$ or, alternatively, assuming a constant gate voltage V_G. Applying a constant gate current for $t > 0$, the time varying drain current becomes:

$$I(t, I_G) = I_o - I_G\left(f + \frac{t}{\tau_e}\right). \tag{18}$$

Here, $I_o = G\cdot V_D$ is the drain current at steady state (i.e. for $I_G = 0$)

and $\tau_e = \frac{ep_o v}{V_D G} = \frac{L^2}{\mu V_D}$ is the time constant of the electronic system.

This relation provides a straightforward means to extract the effective hole mobility in the semiconductor film. Bernards and Malliaras indeed used this relation to predict hole mobility of PEDOT:PSS near the Fermi level from the extracted τ_e and showed that the results are in agreement with literature values[71,72] (cf. Figure 4a).

In the other limiting case a voltage step function V_G is applied to the gate. In this case, the change in cations inside the PEDOT:PSS layer $\frac{dQ}{dt}$ is determined by charging the gate capacitor C_G through the ionic resistance of the electrolyte R. It follows:

$$Q(t) = Q_{ss}\left(1 - e^{-\frac{t}{\tau_i}}\right) \tag{19}$$

where $\tau_i = RC$, is the capacitive charging time constant. In the linear regime, i.e. before the channel is pinched off, the transient current can be calculated assuming an average voltage drop across the gate capacitor of $\Delta = V_G - \frac{1}{2}V_D$ as:

$$I(t, V_G) = I_{ss}(V_G) + \Delta I_{ss}\left(1 - f\frac{\tau_e}{\tau_i}\right)\exp\left(-\frac{t}{\tau_i}\right) \tag{20}$$

where subscript "ss" signifies steady-state currents and $\Delta I = I_{ss}(V_G = 0) - I_{ss}(V_G)$.

Depending on the relative magnitudes of f, τ_e and τ_i, two qualitatively different responses are predicted when applying a gate voltage pulse: a monotonic decay or a spike-and-recovery type response (cf. inset Figure 4b). Neglecting the voltage dependence of the double layer capacitance formed between the semiconductor and the electrolyte, and assuming a linear conductivity of the ionic solution, one finds that $\tau_i \sim l/C_o^{1/2}$,[73] where l is the length of the electrolyte and C_o is the ion concentration. This leads to a ratio of $\tau_e/\tau_i \sim L^2 C_o^{1/2}/l\mu V_D$, which determines which time constant dominated the transient behavior. Bernards and Malliaras varied V_D to tune this ratio and operate the transistor in the two characteristic regimes and as seen in Figure 4b.

2.3 Other Modified Equivalent Circuit Models: Transient Behavior of OECTs.

Several authors proposed improvements to the transient model of Bernards et al.[51] Most importantly, they improve the model by reducing the error introduced by averaging holes and ion currents along the transistor channel (cf. Equation 15) and to find a physical interpretation for the ad-hoc constant f introduced in Equation 16. For example, Gentile et al.[74] interpreted f as the fraction of the penetration depth of ions into the semiconductor over the total thickness of the semiconducting layer.

Friedlein et al.[75] described a first attempt to introduce a (simplified) spatial dependence of the transient gate current. He modeled the ionic gate current by an equivalent circuit that explicitly separates capacitive gate coupling to the source and drain electrode.

Faria and co-workers extended this concept and defined the factor f as the fraction of gate currents that flows to the drain.[76,77] Accordingly, the time dependence of drain current can be separated into three different contributions as in Equation 21 below (cf. Figure 5c).

$$I_D(t) = I_o - \hat{f}\cdot I_G(t) + \Delta I_{ch} = I_o - \hat{f}\cdot I_G(t) \pm g_m V_{ch}(t) \tag{21}$$

The first contribution, I_o, is the steady-state drain current, which is a function of device dimensions and the channel material.

$I_G(t)$ is the transient gate current flowing in response to a change in the gate potential. As discussed above, the factor $\hat{f}$ defines the fraction of gate current flowing towards the drain electrode, while the remaining fraction of the gate current, $(1-\hat{f})I_G$, flows towards the source and does not contribute to the drain current. This contribution to the drain current is short-lived and relaxes to zero ones the device reaches its steady state. Finally, $\Delta I_{ch} = g_m V_{ch}$ is the change of the steady-state drain current in response to the change in potential measured directly at semiconductor/electrolyte interface V_{ch}. Here, g_m is the transconductance of the device, i.e. $g_m = \frac{\partial I_{DS}}{\partial V_{in}}$.

V_{ch} is not experimentally accessible, but to calculate it from the potential applied to the gate, Faria proposed a slightly adapted equivalent circuit shown in Figure 5b. In this circuit, R_d and C_d represent the resistance and capacitance of the transistor channel, respectively, while the resistance of the electrolyte solution is modelled by a linear resistance R_s. Faria et al. were able to obtain a general solution for I_G and V_{ch}, and thereby I_D, in response to a voltage step function applied to the gate $V_{in} = V_o\varepsilon(t)$

$$I_D(t) = I_D + \frac{V_o(g_m R_d - 1)}{R_d + R_s} - \frac{V_o R_d(g_m R_s + 1)}{R_s(R_d + R_s)} exp\left(-\frac{R_d + R_s}{C_d R_d R_s}t\right) \tag{22}$$

$$\tau = \frac{C_d R_d R_s}{R_d + R_s} \tag{23}$$

Here τ is the time constant of the equivalent circuit proposed by Faria, which is equivalent to the time constant found in Bernards model ($\tau = C_d R_s$) when $R_d \gg R_s$.

Faria et al. used Equation 22 to fit the transient response of regular PEDOT:PSS-based OECT and obtained R_s, R_d and C_d, which were in good agreement with literature values.[60] They furthermore generalized their solution to arbitrary input functions and were able to find the drain current response for an applied simulated action potential. Also, this model was extended to describe the influence of a membrane on the transistor channel, and showed that their results were in qualitative agreement to literature values, indicating that their model could be useful to the OECT bio-sensing community.

In some cases, the transient response of OECTs is asymmetrical, i.e. switching from on-to-off is different to off-to-on[5]. This effect was explained by Ersman et al. by a lateral migration of cations further into the transistor channel or drain electrode not covered by the gate electrolyte[5]. Using carbon electrodes, they were able to minimize this effect, although at the expense of a lower on/off ratio of the devices.

2.4 Model Including Diffusion of Ions: Transient Behavior of OECTs.

All models discussed so far describe the ionic part of the OECT by linear elements, i.e. standard RC circuits. The use of these

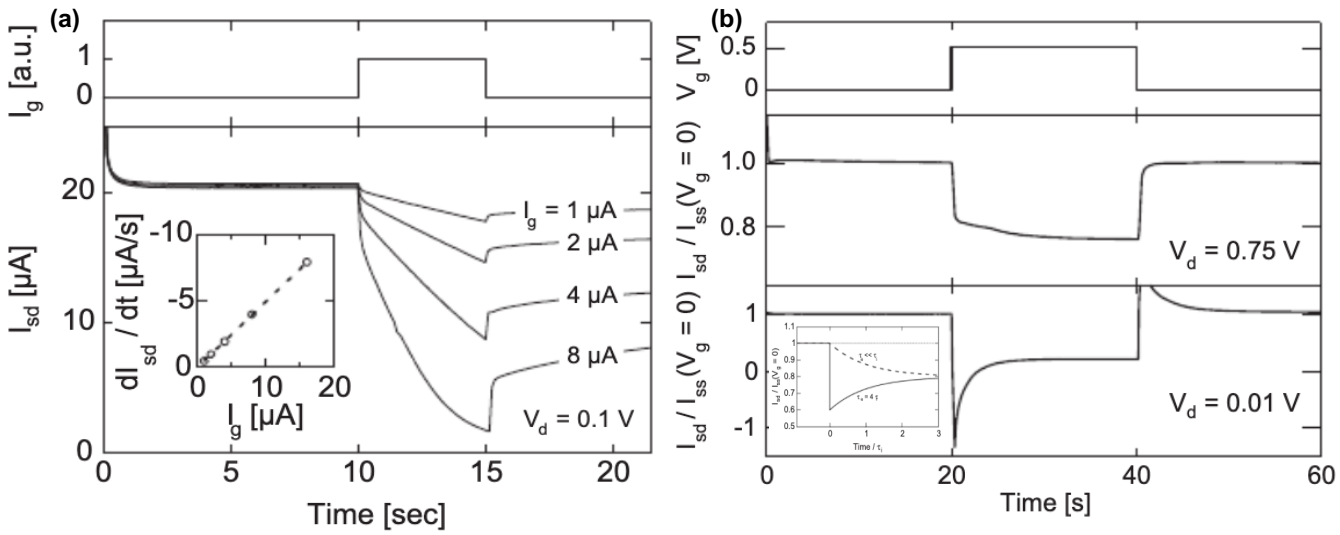

Fig. 4 (a) Experimental transient drain currents of an OECT under application of a constant gate current. The inset shows a plot of the transient slope of drain current versus gate current predicting $\tau_e = 0.5\ s$. (b) Measured transient response of the normalized drain current to the application of a constant gate voltage pulse. Two characteristic responses can be observed for different drain potentials. Inset shows modeled source-drain current transient for a constant drain voltage with an arbitrary ΔI and fixed geometric factor (f = 1/2) showing two different possible characteristics responses. Copyright 2007 WILEY-VCH Verlag GmbH & Co. KGaA, Weinheim.[51]

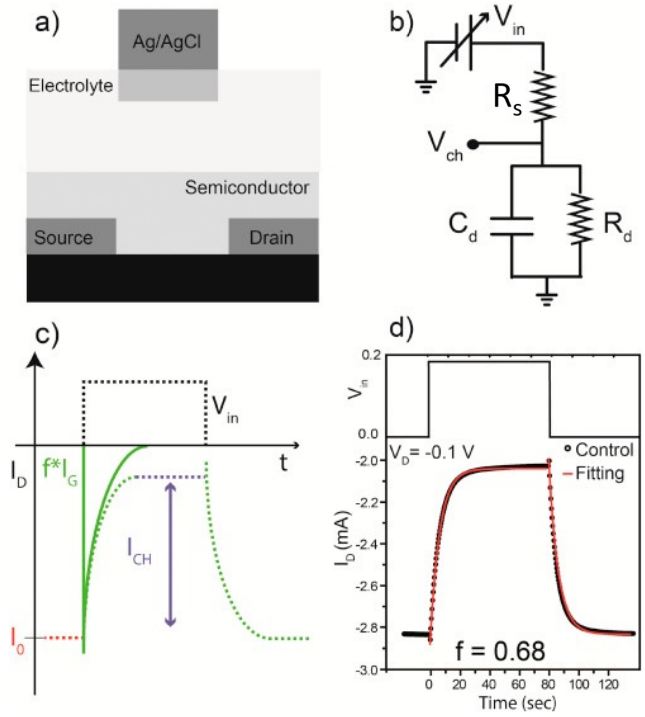

Fig. 5 (a)Schematic diagram of a typical OECT device, (b) the corresponding equivalent circuit, (c) the individual current sources that contribute to the observed drain current and (d) a collected drain current measurement fitted to the transient response model. Copyright Materials Research Society 2014.[77]

equivalent circuits is capable of modeling electric drift of the ions, but neglects diffusion.

Coppedè et al.[78] addressed this shortcoming and developed a model that explicitly includes the diffusion of ions in the electrolyte to determine the transient response of OECTs. This model was used to selectively sense different analytes in a complex mixture.

In this model, it was assumed that a step gate voltage is applied. Later on, Gentile and colleagues[74] extended this work and proposed a model that can be used for periodic driving as well. The model combines elements of the original Bernards-Malliaras model[51] and uses an equivalent circuit similar to the one proposed by Faria et al.[77] However, the resistor R_d (cf. Figure 5b) introduced by Faria et al.[77] is replaced by the Warburg impedance R_W, which depends on the diffusion constant (cf. Figure 6).

In effect, the ionic system is described by a Randles circuit, i.e. it is assumed that the rate of oxidation or reduction is limited by the limited diffusion of ions toward the interface. One obtains an expression for the diffusion resistance R_W[79,80]

$$R_W = \mathscr{T} \cdot \frac{1-j}{\sqrt{\omega}} \tag{24}$$

where ω is frequency of the driving voltage, $j = \sqrt{-1}$ is an imaginary unit, and $\mathscr{T}$ is the Warburg coefficient, which depends on temperature Θ, universal gas constant R, Faraday constant F, number of charges involved in the process n, area of the channel/electrolyte interface A, the concentration of ions in the electrolyte C_o, and the Brownian coefficient of diffusion of the considered ions D as:

$$\mathscr{T} = \frac{R\Theta}{n^2F^2AC_o}\left(\frac{2}{D}\right)^{\frac{1}{2}}. \tag{25}$$

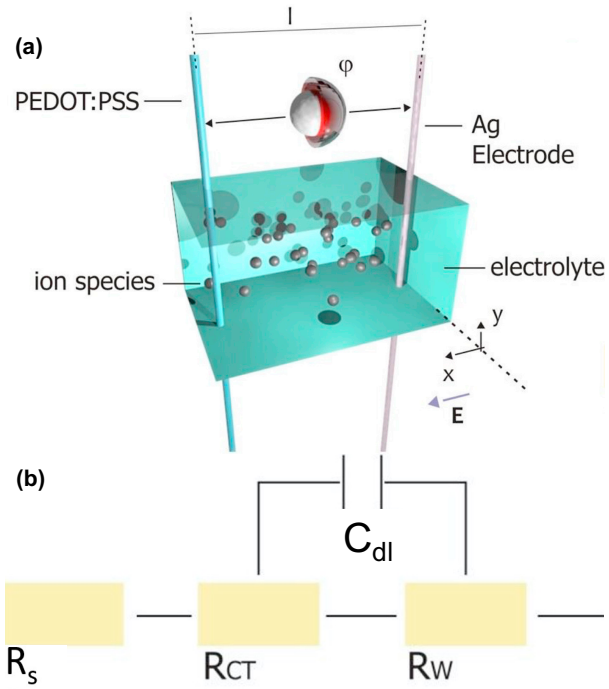

Fig. 6 (a) Device model proposed by Gentile et al consisting of a silver electrode and a PEDOT:PSS polymer embedded into an electrolyte. (b) Equivalent ionic circuit used to describe the transport of ionic charge. Here R_s is the resistance of the electrolyte, R_{CT} is the charge transfer resistance, R_W is the Warburg or diffusion impedance, and C_{dl} is the double layer capacitor. Copyright 2016 Elsevier B.V.[74]

Equation 24 shows that the Warburg impedance combines two components - a purely resistive and a purely imaginary term.

Using the Warburg resistance, the equivalent impedance of the ionic circuit becomes

$$Z_{eq} = \Xi + \Gamma j \tag{26}$$

where

$$\Xi = R_s + \frac{\mathscr{T}}{\sqrt{\omega} + 2C_{dl}\mathscr{T}\omega + 2C_{dl}^2\mathscr{T}^2\omega^{\frac{3}{2}}} \tag{27}$$

and

$$\Gamma = -\frac{\mathscr{T}\left(2C_{dl}\mathscr{T} + \frac{1}{\sqrt{\omega}}\right)}{1 + 2C_{dl}\mathscr{T}\sqrt{\omega} + 2C_{dl}^2\mathscr{T}^2\omega}. \tag{28}$$

This equivalent impedance results in a new expression for the time dependent charge $Q(t)$ injected into the PEDOT:PSS channel as described by Equation 29.

$$Q(t) = \int_0^t \frac{V_G(t)}{Z_{eq}}\, dt \tag{29}$$

Equation 29 can be introduced into Equation 17 used in the original Bernards model[51] to obtain the transient drain current for an alternating gate voltage V_G, which, however, takes diffusion of ions into the semiconductor into account as well. The proportionality constant f, which was introduced to correct for the spatially non-uniform hole distribution in the channel, was assumed to depend on the channel thickness T and the penetration depth of ions into the channel leading to $f \sim \frac{\sqrt{\frac{D}{\omega}}}{T}$.

The authors calculated the drain current for a triangular gate voltage with a frequency spanning from 0.01 Hz to 100 Hz. They demonstrated that the time evolution of the drain current depends on the particular ion species (charge, size and diffusivity) and the operating frequency. They observed two different regimes: a high frequency regime where device is resistive, i.e. the drain current follows the change in applied voltage; and a low frequency regime, where current due to dedoping of the PEDOT:PSS film balance purely Ohmic currents.

The model was verified by a comparison to experimental data. These experiments open the possibility to extract the type of ionic species type and its concentrations. Still, the proportionality constant f remains only vaguely defined, and more detailed models are necessary to treat the spatial variations correctly.

3 Equilibrium Models

Capacitive models as described above are used to describe both steady state and transient behavior of OECTs.[54,55,69] In these models[51,59,60,81] the ion concentration along the channel $Q(x)$ is calculated as a function of gate capacitance and applied gate potential as given in Equation 2, which leads to a hole concentration $p(x)$ as described by Equation 5. However, this approach implicitly confines ion transport to the dimension perpendicular to the channel. However, ions are expected to move laterally inside the channel as well, i.e. along the electric field caused by the drain potential.[5]

The effect of neglecting lateral ion currents is shown in Figure 7a, which plots hole concentration, ionic concentration and the corresponding electric fields of a hypothetical transistor calculated from Bernards model and assuming a gate capacitance (c.f. Equation 1). Figure 7b plots hole drift currents, ionic drift currents and ionic diffusion currents resulting from Figure 7a. Although the normalized hole current is constant along the channel, the ionic drift and diffusion current increase. A change in ion current along the transistor channel indicates that ions arbitrarily accumulate in the channel, or, in other words, that capacitive models do not represent a steady-state solution.[82] Neglecting lateral ion currents in capacitive models leads to a non-equilibrium ion distribution along the channel and hence a non-equilibrium hole and potential distribution along the channel as well.

Experimentally, Kaphle et al.[82] used potential probes to measure the electric potential along the channel and compared their result to predictions of standard capacitive models. It was found that the experiment cannot be reasonably fitted by capacitive models. Similarly, Szymanski et al.[83] showed that the ion concentration along the channel differs from the predictions from capacitive models when ion movement along the channel is not restricted in lateral direction. Consequently, predictions taken from capacitive models have to be interpreted carefully, as they do not necessarily correspond to the equilibrium state of the device.

In 2008, Prigodin and co-workers[64] proposed an alternative analytical model of OECTs that is based on the assumption of a constant electrochemical potential of ions inside the mixed conductor, i.e. this model explicitly solves for the steady state distribution of ions and holes along the transistor channel. Assuming that the hole p and cation p_{ion} concentration are related to the

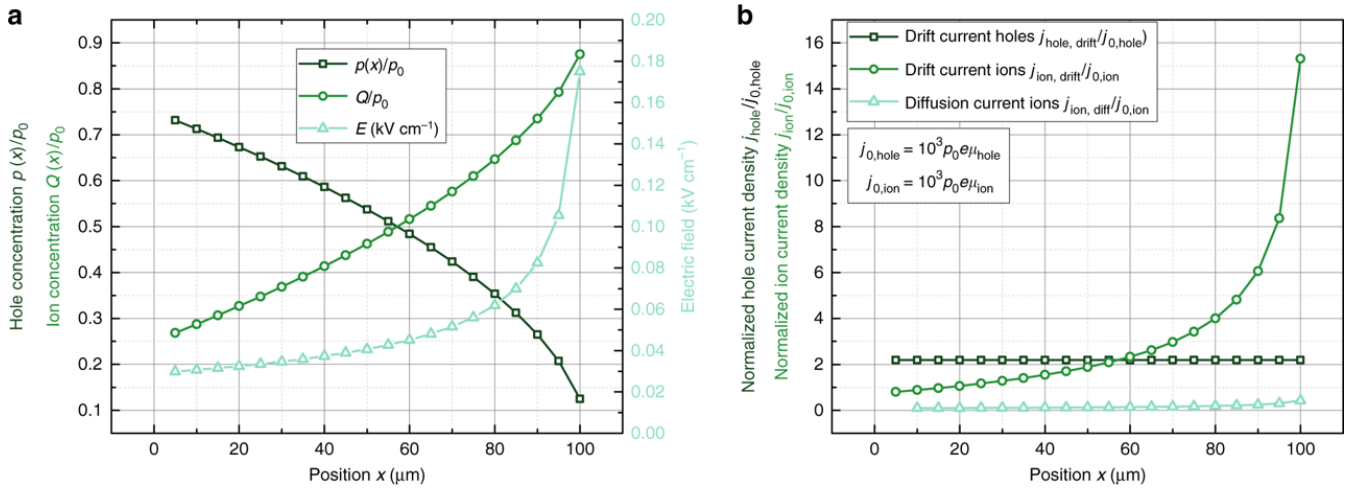

Fig. 7 (a) Normalized hole density, ion density, and electric field inside a hypothetical p-type OECT ($W = 1\ mm,\ T = 200\ nm,\ L = 100\ \mu m,\ p_o = 1020 cm^{-3},\ \mu_{hole} = 0.25\ cm^2\ (Vs)^{-1},\ V_G = 0.2\ V,\ V_D = -0.5\ V$). (b) Normalized hole current, ionic drift current and ionic diffusion currents for charge distribution plotted in (a) calculated using Einstein's equation. Copyright Kaphle et al. 2020.[82]

chemical potential ξ_p, ξ_{ion} of holes and ions by

$$p_{ion} = p_{ion,0} \exp\left(\frac{\xi_{ion}}{k_B T}\right) \tag{30}$$

$$p = p_0 \exp\left(\frac{\xi_p}{k_B T}\right), \tag{31}$$

they derived the following relation of the potential inside the transistor channel $\phi(x)$ on the gate potential V_G, drain current I_D, and diffusion constant of holes D:

$$\exp\left(\frac{e\phi(x)}{k_B T}\right) = \frac{1}{p_0 + p_{ion,0}} \left[p_0 + p_{ion,0} \exp\left(\frac{eV_G}{k_B T}\right)\right] \exp\left(\frac{I_D x}{D(p_0 + p_{ion,0})}\right) \tag{32}$$

Equation 32 is markedly different to the potential distribution expected for capacitive models (see e.g.[82]). In particular, $\phi(x)$ depends linearly on x, and it follows that $\frac{d^2\phi}{dx^2} = 0$.

Integrating the potential along the channel leads to the IV characteristic $I_D(V_D, V_G)$ of the transistors

$$I_D(V_D, V_G) = I_0 \left(1 + \frac{p_{ion,0}}{p_0}\right) \ln\left[\frac{\exp\left(\frac{eV_D}{k_B T}\right) + \frac{p_{ion,0}}{p_0} \exp\left(\frac{eV_G}{k_B T}\right)}{1 + \frac{p_{ion,0}}{p_0} \exp\left(\frac{eV_G}{k_B T}\right)}\right], \tag{33}$$

with $I_0 = \frac{k_B T}{eR_0}$ and R_0 the resistance of the transistor channel without gate voltage applied.

Similar to conventional transistor models, Equation 33 results in a linear and a saturation regime. For small V_D, i.e. in the linear regime, the channel conductance G becomes

$$G = \frac{\frac{1}{R_0}\left(1 + \frac{p_{ion,0}}{p_0}\right)}{\left[1 + \frac{p_{ion,0}}{p_0} \exp\left(\frac{eV_G}{k_B T}\right)\right]}, \tag{34}$$

whereas for $V_D > V_{DS,sat} = V_G + \frac{k_B T}{e} \ln\left(\frac{p_{ion,0}}{p_0}\right)$, the drain current saturates at

$$I_{D,sat} = -I_0 \left(1 + \frac{p_{ion,0}}{p_0}\right) \ln\left[1 + \exp\left(\frac{-eV_{DS,sat}}{k_B T}\right)\right] \tag{35}$$

Although the model of Prigodin correctly describes the OECT behavior under the assumption that ions are at their equilibrium along the transistor channel, it has not been used frequently in the field. In fact, Prigodin et al. stated in their original publication that Equation 33 is not sufficient to explain the full switching operation of their transistors and postulated an additional influence of the injected ions on the hole mobility in the organic semiconductor.[64]

In parallel to this analytical model, several authors numerically solved the continuity equation of ions in two dimensions,[82,84] yielding 2D drift diffusion models of OECTs.[78,85,86]

Shirinskaya and co-workers[86] calculated the density of oxidized and reduced PEDOT:PSS by Nernst's equation, and used the Poisson's equation to determine the potential. Assuming electrical neutrality they were able to study the ion and hole concentration and the electric potential in a 1D electrolyte capacitance. Using this hole concentration, the authors are able to calculate the variation in conductivity along the transistor channel and hence the drain current at different drain-source and gate-source potential. Overall, they were able to reproduce experimentally measured profiles of OECT devices.

Similarly, in 2014 Coppedè et al.,[78] reported a model that solves the transient transport of ions inside the transistor electrolyte, which allowed them to calculate the density of ions injected into the organic semiconductor and by the drain current. Their model was used to discern between different ionic species for sensor applications.

However, in these two models the coupling between the two dimensions of the transistor, i.e. along and perpendicular to the transistor channel, is still weak. Therefore, these two models will suffer the same limitations as capacitive models and are not capable of treating lateral ion currents that equilibriate the electro-

chemical potential of cations.

No attempt to model the movement of ions along the lateral dimension i.e. along the length of the channel was done until Szymański et al.[83] reported on a 2D simulation of OECTs. Inspired by promising results obtained in a related problem of electrochemical doping in organic materials,[87] they successfully used a drift-diffusion model implementing Poisson-Nernst-Planck equations[88] as a careful extension of previous works[89] on modeling electronic devices with ionic transport.[88,90] Results of calculations for steady-state, transient, and AC simulations of the organic electrochemical transistor were presented using realistic materials parameters and the results were validated with experiments. Szymański et al. found that the electrical double layer at the electrolyte/semiconductor interface is essential to understand the working mechanism of OECTs. Furthermore, it was shown that the ion distribution inside the channel will be altered by laterally moving ions.

Recently, Kaphle et al.[82] presented another 2D drift- diffusion model of p-type depletion OECTs. They showed that capacitive models do not describe potential profiles along the transistor channel correctly, but were able to fit the measured electric potential by their 2D drift-diffusion model. Their results suggest that the steady-state ion concentration follows an exponential distribution if the ions are allowed to move laterally under the influence of source-drain potential.

Their interpretation of the device mechanism is slightly different to the mechanism proposed by capacitive models. The injection of ions into the semiconductor is not governed by the difference of the gate and channel potentials (cf. Equation 2), but is a result of the balance between drift and diffusion of cations inside the semiconductor.

Due to lateral ion currents in the device, cations tend to accumulate at the drain electrode of the OECT. This tendency shifts the focus of the working mechanism of the device away from the bulk organic semiconductor to the organic semiconductor–drain electrode interface. As discussed below, this accumulation of ions at the electrodes could be seen as a contribution to the contact resistance observed in some devices.

The 2D drift-diffusion model of Kaphle et al. was used as well to explain the observed bell shaped dependence of transconductance on gate potential and its scaling laws with device geometry.[84] A well defined peak in transconductance is observed at some gate voltage $V_{G,max}$. This particular voltage, $V_{G,max}$, depends on the device dimensions and drain potential. The position of peak shifts towards more negative gate voltages for stronger drain bias (more negative with reference to source). Furthermore, the maximum transconductance increases exponentially on drain potential. The presence of parasitic resistance leads to the departure from linear dependence of $g_{m,max}$ on geometrical factor $\frac{W \cdot T}{L}$ to exponentially saturating dependence. This saturation is more severe for weaker drain bias.

In most drift-diffusion models used to predict OECT behavior[64] and to explain charge transport in organic conjugated polymers,[91,92] electronic and ionic charge carriers are considered to move in the same phase, i.e. both charge species are experiencing the same electric potential. In contrast to these single phase models, Tybrandt et al.[85] proposed that there is a spatial separation between a conjugated polymer (CP) and poly-electrolyte (PE) part of the polymeric semiconductor, with electric charge transported along the CP phase and ions in the PE phase. Hence, in their drift-diffusion model of hydrated CP-PE blends, Tybrandt et al. introduced two distinct electrostatic potentials for the electronic and ionic phases. Consequently, the capacitive behaviour can be explained in terms of electric double layers (EDLs) formed between the CP and PE phase. Overall, this model indicates that CP-PE blends have to be treated as a two-phase system consisting of a semiconducting phase embedded in a matrix of PE. The volumetric capacitance observed in OECTs (cf. Fig 3) is therefore a direct consequence of the three dimensional intermixing of the two phases, leading to an electrostatic potential difference between the electronic and ionic phases resulting in an EDL. The model was shown to fit well with the observed current voltage characteristics of PEDOT:PSS based OECTs.

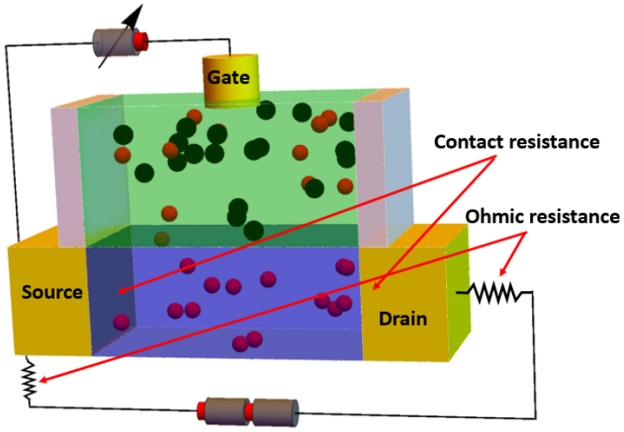

Fig. 8 Cartoon of Organic Electrochemical Transistor showing parasitic resistance.

4 Other Modelling Considerations

4.1 Parasitic Resistance

In all OECT models discussed so far, the source and drain contacts were assumed to be ideal and the drain current is entirely determined by the channel resistance. However, in reality, parasitic series resistances exist which are caused by imperfect injection or extraction at the source and drain contacts (cf. Figure 8). When these parasitic contact resistances have a significant contribution to the total resistance of the device, they will degrade the device performance and can lead to inaccurate estimation of device and material parameters e.g. carrier mobility.

There are two different contributions to the parasitic resistance. One is an obvious Ohmic resistance of the metallic interconnect lines between the power supply and the source/drain electrodes. For example, Donahue et al.[26] showed that the line resistance is significant in case of short channels and large $\frac{W \cdot T}{L}$ ratios. In particular for highly conductive materials such as PEDOT:PSS, which is often treated to improve its conductivity further by several orders of magnitude,[93] the resistance of leads might be a significant factor.

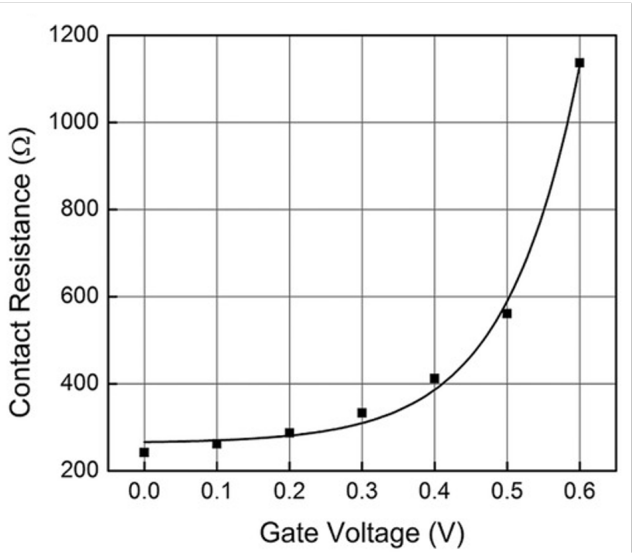

Fig. 9 Contact resistance with respect to gate voltage. The dependency of the contact resistance can be fitted by an exponential dependency: $R_C = A \times exp(B \times V_G) + C$ where A, B and C are fitting parameters that in general depend on the OECT geometry and materials used. Copyright © 2016 WILEY-VCH Verlag GmbH & Co. KGaA, Weinheim.[93]

A second parasitic resistance is the contact resistance that originates from the polymer electrode interface. Contact resistances in OECTs were first reported by Kaphle et al. in 2016.[93] They used two different formulations of PEDOT:PSS and showed that the effect of contact resistance is severe in the case of highly conducting channel materials. Contact resistance measured by the transmission-line method (TLM) measurements of OECTs was found to depend on gate voltage. With the help of the contact resistance, the authors were able to explain the non-monotonic dependence of transconductance on gate voltage and an empirical model for its dependence on gate voltage was proposed as shown in Figure 9.

In contrast to these studies, Friedlein et al.[94] found that contact resistance is only a secondary cause for the non-monotonic transconductance and argued that the energetic disorder of the polymeric semiconductor is the primary cause of bell-shaped dependence of transconductance on gate potential.

The origin of the contact resistance in OECTs is currently not well understood. In OFETs, the contact resistance is mainly due to injection barriers at the source contact and misalignment of the energy levels at the metal/semiconductor interface.[95,96] Thus, in OECTs a mismatch in energy levels of the polymer and electrode materials might cause the contact resistance. This, however, does not entirely explain the exponential dependence of the contact resistance on the gate voltage. Recently, Kaphle et al.[82] proposed that the accumulation of cations at the drain electrode due to lateral drift of ions along the channel leads to a parasitic voltage drop at the channel/drain interface that can be modeled by a contact resistance. Paudel et al.[84] performed similar 2D calculations and showed additional series resistance explains the observed saturation of transconductance on the device geometry $\frac{W \cdot T}{L}$ (cf. Figure 10a). Similar effect of contact resistance on transconductance was previously reported (cf Figure 10b[55] using Bernards Model[51] as well.

In addition to lowering the transconductance, contact resistance is also predicted to shift the gate voltage corresponding to the peak transconductance to more positive voltages.[55]

The influence of contact resistances goes beyond a reduction in transconductance. In 2017, Stoop et al.[97] studied the signal-to-noise ratio (SNR) of OECTs and found that the contact resistance increases the noise level and suggested to use large-area polymer channels to maximize the SNR.

Later on, it was found that the overlap area of the source/drain contact with the organic semiconductor[98] does not influence the steady-state transconductance and noise, but changes the frequency response of the device. This shows contact resistance is independent of the overlap area and is a function of materials and charge injection contacts.

Various techniques are known to reduce contact resistance in OFETs,[99–102] but not all of these methods are applicable to OECTs. The injection into n-type OECTs was optimized by adding two different thiol based self assembled monolayers (SAMs)[103] on the gold electrodes. It was reported that 4-methylbenzenethiol (MBT) SAM enhances overall performance whilst pentafluorobenzenethiol (PFBT) has an opposite effect on transconductance. As both SAMs were shown to decrease the contact resistance, contact resistance is not seen to be the only factor influencing the transconductance. A study of the surface energy and topography of the polymer films revealed that the semiconductor solution preferentially wets the MBT functionalized gold electrodes, but does not cover untreated gold completely. This also has a positive impact on the quality of semiconductor film-formation in the channel.

A scanning probe setup using scanning electrochemical microscopy (SECM) to obtain the local electrochemical potential of the device channel and electrolyte was used by Mariani et al. along with a model to relate measured potentials to local carrier concentration, charge carrier mobility and contact resistance for OECTs.[104] This technique is versatile and can directly measure device operation providing a non-destructive way for a direct assessment of the device performance. They observed a step in the potential at the source/drain contacts in the form ΔV_c (cf. Figure 11) similar to the findings of Kaphle et al.,[93] who related this drop to the contact resistance R_c.

4.2 Future directions in OECT Device Modelling

Our understanding of OECTs has rapidly grown in the past decade and still continues to improve. However, despite this progress, the goal of a quantitative and predictive OECT model has not yet been reached. There are several key questions that are still unanswered and have to be addressed.

Most importantly, more morphological studies have to be performed to understand the different ion and hole conductive phases inside mixed conductors, and to decide if a homogeneous device model is sufficient to capture OECTs correctly, or if complex multiphase structures have to be incorporated into the models.

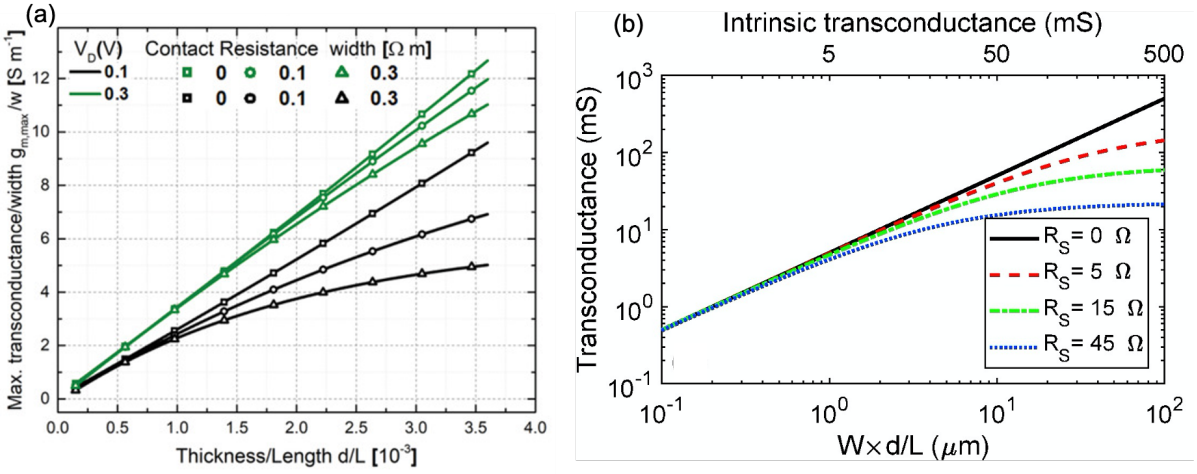

Fig. 10 Reduction in transconductance with parasitic series resistance. (a) Simulated result for a maximum transconductance as function of device geometry T/L using 2D model.[82] Copyright 2020 Wiley-VCH GmbH.[84] (b) Effective transconductance as a function of channel geometry (bottom axis) and intrinsic transconductance (top axis) for series resistance at the source electrode of (solid black line), (dashed red line), (dash-dotted green line), and (dotted blue line). The results shown are for an OECT simulated according to the Bernards model[51] with hole mobility $\mu = 2\ cm^2V^{-1}s^{-1}$, volumetric capacitance $C^* = 50\ F\ cm^{-3}$, threshold voltage $V_T = 0.5\ V$, applied voltages $V_G = 0\ V$ and $V_D = -0.6\ V$. Copyright 2018 Friedlein et al.[55]

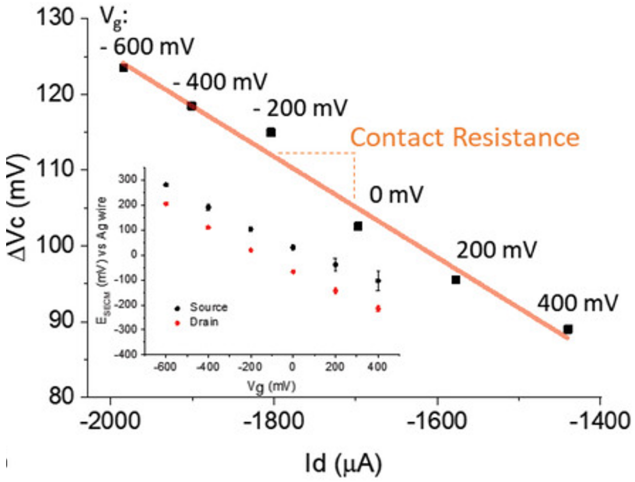

Fig. 11 Drop in electric potential at the source/drain contact (ΔV_c) in dependence of the drain current at different gate biases. The points scale linearly with the OECT channel current, indicating an Ohmic behavior of the contact resistance. The inset shows ΔV_c values calculated from E_{SECM} measured on source and drain contacts. Copyright © 2019 WILEY-VCH Verlag GmbH & Co. KGaA, Weinheim.[104]

Similarly, except for the model of Shirinskaya,[86] the de-doping mechanism inside the mixed conductor is modeled in a highly simplified way as a purely electrostatic process, neglecting the detailed balance between the oxidized and reduced form of PEDOT:PSS. More sophisticated models have to be found, in particular to capture the transient response of OECTs better.

Furthermore, the precise coupling between ion and hole mobility is not understood. First results of Friedlein et al.[94] already showed that the hole mobility is not constant, but most likely depends on ion and charge concentrations. Similarly, Prigodin et al. described a mechanism to explain a change in hole mobility due to the presence of ions.[64] A microscopic understanding of hole and ion transport in mixed conductors has to be found before OECT models can be expected to become predictive.

Finally, ion accumulation at the source and drain electrode of the OECT will influence charge injection and extraction significantly. Models that describe charge injection in the presence of a large ion concentration have to be found.

5 Materials Design for OECTs

5.1 Channel Materials.

5.1.1 General Overview.

As previously discussed, our understanding of the working mechanisms of OECTs is still evolving and a predictive device model has still not been found. Although this lack in detailed understanding makes it challenging to formulate precise design rules for high-performing OECT materials, our current level of understanding is sufficient to guide further materials development.

As shown in the discussion of the Bernards and Malliaras model, the transconductance g_m of the transistors in the saturation regime becomes[54]

$$g_m = \frac{W}{L} T \mu C^* (V_{th} - V_G), \tag{36}$$

i.e. the transconductance scales with the geometric factor $g_m \propto \frac{W}{L}T$. This scaling law is in fact not bound to capacitive models, but is found for equilibrium models as well.[84] Therefore, the materials dependent factor of Equation 36, μC^*, is used as figure of merit that is optimized for new materials. It combines the hole or electron mobility μ, describing the efficiency of charge transport, with the volumetric ionic capacitance C^*, describing the effectiveness of ions to penetrate the semiconductor and control the drain current.

The figure of merit μC^* is a good design target to optimize the steady state performance of OECTs; for transient studies, though, it is more difficult to define a clear target. Following the dis-

cussion in Section 2.2, the ion diffusivity in both the electrolyte and the semiconductor, as well as the hole/electron mobility in the semiconductor have to be maximized. The diffusion constant of ions inside the semiconductor can be increased by hydrophilic side-groups[105], which results in more water uptake during operation of the OECT. However, too much water uptake results in excessive swelling of the films, which disrupts electronic transport and hence lowers the hole mobility.[105] Therefore, synergistically optimizing the ion and the electron/hole mobility in the semiconductor might not be possible. Instead, a compromise between ion and hole/electron mobility has to be found that results in an optimized response speed.

Attempts have been made to increase the product of electron mobility μ and volumetric ionic capacitance C^* through materials design. Since the first demonstration of polypyrrole (PPy) as a polymeric organic semiconductor in an OECT in 1984,[106] early channel materials were primarily derived from homopolymers such as PPy, PANI, and PEDOT. Advancements in molecular design have dramatically expanded the scope of available structures, chemical functionality, and monomer sequencing, thereby improving the performance of the channel material. While the majority of OECTs reported utilize PEDOT:PSS as the active layer, recent efforts have demonstrated solution-phase chemical approaches to diversify the polymer structure and fine-tune the properties of the channel material through the use of backbone and side-chain engineering.

In this section, progress in materials design for OECT technologies will be reviewed, with a particular emphasis on systematic structural modifications that can be utilized to understand structure-function-property relationships and better articulate important material design parameters (Figure 12). Examples of contemporary high-performance donor-acceptor (D-A) copolymers are highlighted to illustrate design features developed from the OFET and organic photovoltaic (OPV) communities. Overall, these simple design features and guidelines have led to impressive progress in the design of new materials. For perspectives on early active material design and optimization of PEDOT, the reader is directed to prior accounts.[107,108]

5.1.2 Backbone Engineering.

Channel materials typically consist of an organic semiconductor synthesized by electrochemical or wet-chemical methods. While OECTs can be subdivided based on their p- or n-type transport behavior, or the accumulation or depletion mode of operation, only the transport behavior is directly related to the backbone architecture.

While early demonstrations utilized polypyrrole (PPy) and polyaniline (PANI), the introduction of poly(styrene-sulfonate)-doped poly(3,4-ethylenedioxythiophene) (PEDOT:PSS) as an active material in 2002[109] has resulted in its broad adoption and to date is the most widely utilized OECT material on account of its widespread commercial availability, processability, and high conductivity (Figure 13). While the use of PEDOT has enabled significant growth in OECT research, the polymer is synthetically challenging to modify, making the systematic control of important device parameters challenging. Several strategies have been proposed to overcome the various limitations of PEDOT:PSS through creative dopant and blend design,[23,110–113] however many bulk properties are intrinsic to the molecular architecture of the polymer.

Recent work has focused on the development of both p- and n-type semiconducting materials through backbone engineering, with a particular focus on p-type materials largely comprised of thiophene structural units.

5.1.3 P-type Semiconductors

Since the first demonstration of increased conductivity of a polythiophene (PT) material upon iodine doping in 1980,[114] PTs have played a major role in the field of organic electronics and have found widespread use in transistors due to their thermal and oxidative stability, ease of processing, and high charge carrier mobility.[115] PT materials are rendered conductive through the formation of mobile carriers in the form of polarons and bipolaron upon treatment with a small molecule or polymeric oxidizing agent (p-doping), and have demonstrated the desired compromise between high electronic and ionic transport required for OECTs.

As previously mentioned, the product of the electronic mobility and volumetric charge storage capacity (μC^*) is a useful figure of merit to aid the design of future channel materials for OECTs; and of the ten top performing systems studied, all of them consisted of thiophene derived structural units.[53] A high μ is achieved through a tightly packed, often crystalline, polymer morphology, while a high C^* relies on facile ion migration within the polymer active layer.

The simplest PT structure is a homopolymer with solubilizing chains extending from the π-conjugated backbone, the most extensively studied being poly(3-hexylthiophene-2,5-diyl) (P3HT).[115–117] P3HT has been utilized as the active layer in OECTs,[118,119] however the poor uptake of water, and the relative challenge of electrochemical oxidation and reduction of the polymer in aqueous environments has limited the transconductance of these devices.

While recent reports have demonstrated the use of small molecule additives, ionic liquids, and liquid-liquid phase separation procedures to increase the performance of P3HT and other hydrophobic polymers,[120–122] various monomers have been designed to increase the hydrophilicity of PT materials to allow for swelling and therefore ion penetration in aqueous environments. In 2014, poly(6(thiophene-3-yl)hexane-1-sulfonate) (PTHS), a conjugated polyelectrolyte (CPE) resembling P3HT, but with a hexanesulfonate side-chain, was introduced as the active layer of an OECT.[123] OECTs developed with PTHS demonstrated high transconductance due to the remarkably high hole mobility ($1.2 \pm 0.5) \times 10^{-2}\ cm^2\ V^{-1}\ s^{-1}$),[124] as well as a large volumetric capacitance $124 \pm 38\ F cm^{-3}$.[53] The hydrophilic sulfonate side-chains enabled swelling, and therefore uptake of water molecules and mobile ions leading to improved ionic conductivity when compared with the more hydrophobic P3HT.

Since the initial report utilizing PTHS, sulfonated thiophene structural units have been incorporated into various PT copolymers to increase ion transport. Recently, the ion-conducting 6-(thiophen-3-yl) hexane-1-sulfonate (THS) monomer was copoly-

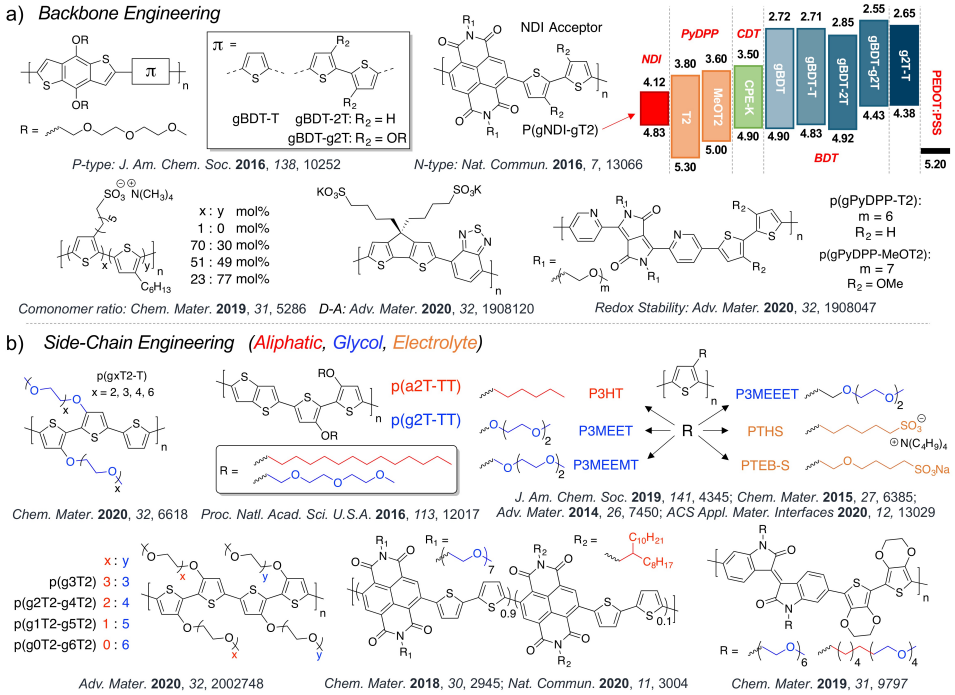

Fig. 12 (a) Representative chemical structures demonstrating examples of backbone engineering. The band diagram illustrates the frontier molecular orbital energies of various active materials reported in the literature, organized by polymer backbone structure. (b) Representative chemical structures demonstrating examples of side-chain engineering. Side-chains are color coded to illustrate chemical identity.

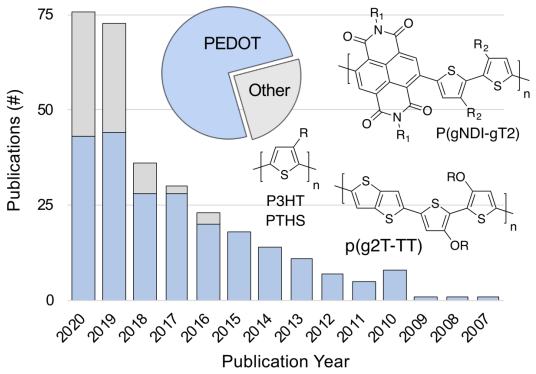

Fig. 13 Total number of publications including the term "OECT" from 2007 to 2020, organized by the structure of the active material. Data was obtained from SciFinder

merized with 3-hexylthiophene (3HT) to obtain copolymers with various gradient architectures (Figure 12a).[125] The sulfonated THS monomers provided water compatibility, swelling, ion uptake, and high volumetric capacitance. The 3HT monomers were important for reducing water solubility preventing film delamination and percluding the use of external crosslinkers, which typically reduce the electrical conductivity of the active layer through changes in film morphology.[126] Through backbone engineering, the copolymers demonstrated synergistic advantages associated with P3HT and PTHS, exhibiting high volumetric capacitance ($C^* > 100\ Fcm^{-3}$), high hole mobility ($\mu = 1.7 \times 10^{-2} cm^2 V^{-1}\ s^{-1}$), a lower threshold voltage ($-0.15\ V$), and higher ON/OFF ratio than PTHS (Figure 14).

The design strategy not only afforded a significant improvement compared to high-performance PTHS, but also offers a simple solution to improve the performance of other hydrophobic materials which lack appropriate ion transport and swelling in aqueous environments. Other sulfonated monomers such as sodium 4-(2-(2,5-bis(2,3-dihydrothiene[3,4-*b*][1,4]dioxin-5-yl)thiophen-3-yl)ethoxy)butane-1-sulfonate (ETE-S) have been used to similar affect in OECTs.[127]

To achieve increased performance in PT based materials, the OFET and OPV communities have taken advantage of fused thiophene derivatives. These building blocks lead to more extended conjugation, planar molecular geometries, and rigid structures that promote efficient intra- and intermolecular charge transport and higher charge mobilities.[115]

In 2016 a series of neutral active materials derived from benzo[1,2-*b*:4,5-*b*]-dithiophene (BDT), a prototypical building block for efficient photovoltaic materials,[128] was used to demonstrate the role of chemical design in the performance of OECTs.[129] Both BDT and 2,2-bithiophene (2T) monomers were functionalized with triethylene glycol (TEG) chains and various copolymer structures were examined including copolymers of BDT-2T and BDT with unsubstituted thiophene and bithiophene structural units (Figure 12a). The series of copolymers demonstrated various degrees of TEG side-chain density, polymer backbone curvature, and ionization potentials ranging from 4.4 to 4.9 eV. While increased TEG side-chain density improved ion transport within the film and decreased ionization potentials (see Section 5.1.5), it was found that the TEG functionalized bithiophene unit (g2T) enabled more electrochemically stable polymers

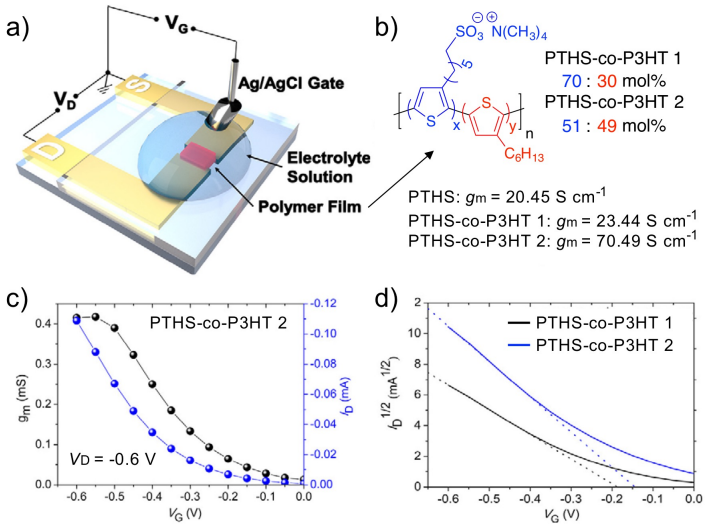

Fig. 14 (a) Schematic of the OECT setup. (b) Chemical structures of PTHS-co-P3HT copolymers with annotated transconductance values. (c) Transfer curve of PTHS-co-P3HT 2 with corresponding transconductance plotted vs. V_G. (d) $I_D^{1/2}$ vs. V_G plots for OECTs comprising PTHS-co-P3HT 1 and 2. Adapted with permission.[125] Copyright © 2019 American Chemical Society.

than those with the TEG functionalized BDT unit. It was hypothesized that the increased electrochemical stability was due to the electron-rich nature of the g2T structural unit, significantly lowering the ionization potential by $0.4-0.5\ eV$.

The efficient charge transport within p(g2T-T) compared to the other polymers of the series was attributed to an edge-on orientation and a planarization assisted by the intramolecular $S-O$ interactions within the g2T structural unit. After device optimization, p(g2T-T) demonstrated the highest reported peak transconductance of above 20 mS with excellent turn-on voltages around $0\ V$, high on/off ratios, and fast temporal responses.

Since this initial report, p(g2T-T) has been a top performing active material for accumulation mode OECTs,[53] and recent reports have focused on further increasing performance through side-chain engineering (see Section 5.1.5),[130,131] and backbone engineering through the incorporation of other fused thiophene derivatives commonly utilized in high-performance OSCs.[132] For example, the highest performing p-type material utilized to date is poly(2,5-bis(3-alkylthiophen-2-yl)-thieno[3,2-*b*]thiophenes) (PBTTT), incorporating fused thienothiophene (TT) structural unit.[133] Since the development of PBTTT by Merck (US patent 7,714,098) and the first report in 2006,[134] it has been utilized as an active material in OECTs.[120,122,135] Through the copolymerization of the fused TT and glycolated g(2T) monomers, poly(2-(3,3'-bis(2-(2-(2-methoxyethoxy)ethoxy)ethoxy)-[2,2'-bithiophen]-5-yl)thieno[3,2-*b*]thiophene) (p(g2T-TT)) demonstrated a remarkably high μC^* of $227 \pm 107\ F\ cm^{-1}\ V^{-1}\ s^{-1}$ compared to that of p(g2T-T) ($62 \pm 24\ F\ cm^{-1}\ V^{-1}\ s^{-1}$), making p(g2T-TT) one of the top performing active materials for OECTs.[53,132] Recently, p(g2T-TT) has been utilized for the investigation of water uptake during device operation,[136] polymer-electrolyte interactions,[137] and electrophysiological sensing via OECTs.[138]

4*H*-Cyclopenta[2,1-*b*:3,4-*b*']dithiophene structural units (cyclopentadithiophene, CPDTs) represent another class of fused thiophene derivatives which have been frequently used as donors in D-A polymers. In contrast to the fused thienothiophene (TT) unit, the sp^3-hypridized carbon atom of CPDT allows the attachment of side-chains above and below the plane of the polymer backbone which enables the tuning of solubility and polymer packing.[115] Cyclopentadithiophene-benzothiadiazole (CPDT-BTZ) D-A copolymers have demonstrated high hole mobilities of ($10\ cm^2\ V^{-1}\ s^{-1}$) and have been extensively investigated and utilized in field-effect transistors,[139,140] bulk heterojunction (BHJ) solar cells,[141] and thermoelectrics.[142] Recently CPE-K, a highly conductive CPDT-BTZ copolymer with sulfonate side-chains was utilized as the active material in an OECT, representing the first CPDT-based polymer for such an application(Figure 12a).[143] The sulfonate side-chains allowed for water and ions to penetrate and drift within the bulk of the film as with other sulfonated active materials, and also acted as a functional handle for (3-glycidyloxypropyl)trimethoxysilane (GOPS), a cross-linking agent which stabilized the otherwise aqueous soluble material. Despite a relatively low volumetric capacitance of $1.34 \times 10^2\ F\ cm^{-3}$, CPE-K-based devices demonstrated comparable transconductance to other common materials under the same device geometries and demonstrated similar performance to PTHS.[53,143] The adaption of a high mobility D-A conjugated polymer to a polyelectrolyte utilizing water soluble side-chains represents a viable method for developing novel materials for OECTs, and represents an alternative approach and paradigm shift from PEDOT:PSS.

Backbone engineering has also been utilized as a tool to increase the redox stability of the active materials within OECTs. Noncapacitive faradaic side-reactions between the active material and the electrolyte can modify the chemical composition of the polymer and significantly decrease the performance of the device. For example, while BDT copolymers have been used to good effect, they were found to be inherently unstable when applied in OECTs.[129]

Recently, a series of alkoxy-BDT copolymers were systematically designed to assess the factors determining redox stability in aqueous electrolytes.[144] Copolymers gBDT-TT, gBDT-T2, and gBDT-MeOT2 were chosen to study the influence of ionization potential (IP) on the electrochemical redox reactions. The 3,3'-dimethoxy-2,2'-bithiophene (MeOT2) structural unit has an electron rich nature and planar structure associated with intramolecular sulfur-oxygen interactions, resulting in an decreased IP for gBDT-MeOT2 (4.31 eV) when compared to gBDT-TT and gBDT-T2 (4.70 and 4.85 eV). The comparatively large IP of gBDT-TT and gBDT-T2 lead to highly oxidizing polarons that result in polymer degradation, while the relatively higher lying HOMO of gBDT-MeOT2 lead to greater electrochemical stability. Spectroscopic measurements demonstrate that the alkoxy-BDT unit of gBDT-TT and gBDT-T2 oxidize at the 4,8-positions to form irreversible irreversible quinone structures, while the alkoxybithiophene unit (MeOT2) demonstrates stable positive charges along the polymer backbone, thereby enabling long-term stability. Each polymer was used as an active material in p-type accumulation mode OECTs, where the varying structural stability between the polymers manifested in significant differences in device performance. For example, gBDT-MeOT2 demonstrated a volumetric capacitance of 95 $F\ cm^{-3}$ at $V_G = 0.6\ V$, while gBDT-TT and gBDT-T2 could not be analyzed by EIS measurements on account of their oxidative instability.

These design principles were recently extended to pyridine-flanked diketopyrrolopyrrole (PyDPP) polymers to enable electrochemical stability in the presence of molecular oxygen (Figure 15a).[145] The electron-transfer reaction from the active material to molecular oxygen, known as the oxygen reduction reaction (ORR), is directly related to the energy levels of the active material and the products of the ORR (Figure 15b).[146] The bithiophene glycolated copolymer p(gPyDPP-T2) has an elevated IP of 5.3 eV compared to that of p(gPyDPP-MeOT2) (5.0 eV). Examination of the orbital and charge distribution along the polymer chains suggested the MeOT2 structural unit provides more localization of the wavefunction and therefore stability for the hole polaron than the T2 unit, thus increasing redox stability of the P(gPyDPP-MeOT2) copolymer. Under long-term pulsed cycling and continuous charging conditions, p(gPyDPP-MeOT2) showed 0%, 8%, and 16% change in ON current after 400 cycles when applying $V_G = -0.5\ V$, $-0.6\ V$, and $-0.8\ V$, respectively (Figure 15c), while p(gPyDPP-T2) had low observed device stability.

The promising ON/OFF ratio ($> 10^5$), normalized peak transconductance ($19.5 \pm 2.5\ S\ cm^{-1}$), and good stability of p(gPyDPP-MeOT2) (Figure 15c), has motivated further investigations into DPP based building blocks for the construction of active materials in OECTs.[147,148] Recently a series of glycolated DPP polymers were synthesized with systematic backbone modifications in order to elucidate structure-property relationships for high-performance D-A channel materials.[148] Three different thiophene-based monomers, the same structural units utilized in the alkoxy-BDT copolymers discussed previously (Figure 12a),[144] were copolymerized with a glycolated DPP unit to afford a series of p-type channel materials for OECTs (Figure 16a). As observed in the pyridine-flanked DPP series,[145] the electron-donating MeOT2 unit reduced the IP when compared to the other units investigated. When incorporated into OECTs, p(gDPP-T2) demonstrated the highest steady-state OECT performance, followed by p(gDPP-TT), and p(gDPP-MeOT2) (Figure 16b). As each polymer demonstrated similar $C^*(\sim 180\ F\ cm^{-3})$ as measured using EIS, the origin of the performance difference between the materials was their differing charge carrier mobilities, which was attributed in part to the higher molecular order in p(gDPP-T2) and p(gDPP-TT). Computational simulations of oligomeric variants of the polymers suggested that the charge was more delocalized and distributed more evenly in p(gDPP-TT) and p(gDPP-T2) than in p(gDPP-MeOT2). The closer energy match between the T2 and TT moieties with the DPP unit, compared to that of MeOT2, may have allowed greater polaron delocalization and increased charge carrier mobility. The authors further hypothesized that closely matching the electron-densities and energy levels of donor and acceptor units may yield better charge transport properties in D-A materials intended for OECTs. Through backbone engineering, building blocks were selected to rationally design materials which compared well with other high-performing systems (Figure 16c), while highlighting principles that may guide the future development of D-A channel materials for OECTs.

5.1.4 N-type Semiconductors

The development of n-type materials has trailed behind their p-type counterparts on account of their instability in ambient conditions. This can be associated with the high reactivity of radical anions in the presence of atmospheric water and/or oxygen. It is therefore unsurprising that the use of n-type active materials within OECTs remains rare,[149] despite significant progress in the realization of various optoelectronic devices and complementary circuits based on these materials.[150,151]

As the redox potential of H_2O is $-0.66\ V$ vs. the saturated calomel electrode (SCE), only n-type organic semiconductors with low lying LUMO energy levels below approximately $-4.0\ eV$ with respect to vacuum are stable in ambient atmospheric conditions. To fulfill these requirements, polymer backbones are functionalized with strong electron-withdrawing groups such as carbonyl, fluorine, cyano, or fluororcarbon groups integrated within fused (hetero)arenes. These design strategies have led to the development of common electron-deficient building blocks such as perylenediimides (PDI), naphthalenediimides (NDI), diketopyrrolopyrrole (DPP), isoindigo (IID), and benzodifurandione (IBDF), among others.[149]

In 2016, a narrow band gap D-A copolymer based on NDI was introduced as a n-type active material for accumulation mode OECTs demonstrating stability in water,[152] and since then has been the primary backbone of interest for such devices.[153–156] A combination of doping energetics within the narrow stability window imposed by water, and a high capacity for electrochemical charge lead to the stable operation of p(gNDI-gT2) in a n-type accumulation mode OECT. Consistent with p-type active materials, it was found that the higher glycol side-chain density of p(gNDI-gT2) compared to that of p(gNDI-T2) lead to enhanced ion injection, while also lowering mobility due to inefficient $\pi-$stacking.

Subsequently, a series of random NDI-T2-based terpolymers

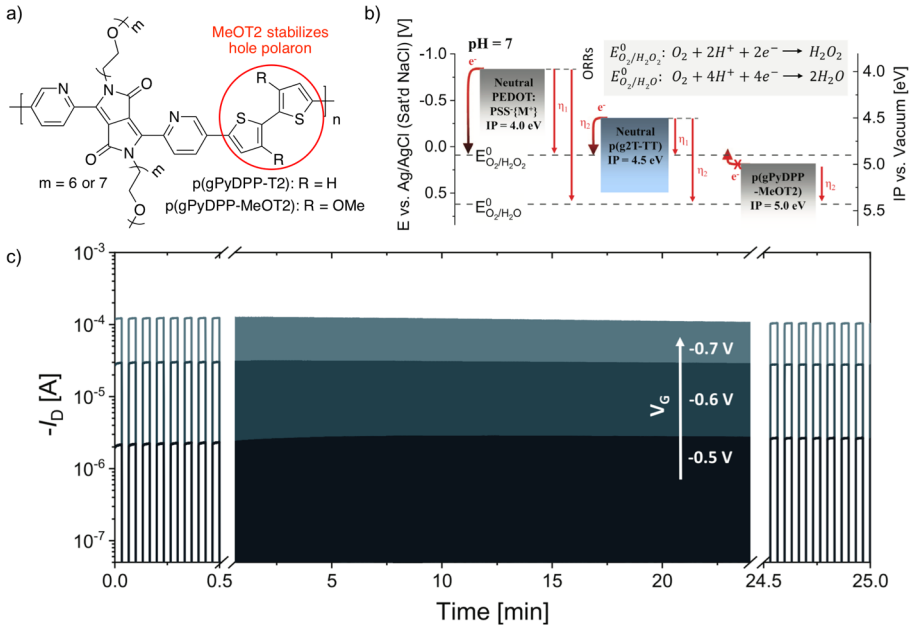

Fig. 15 Chemical structures of p(gPyDPP-T2) and p(gPyDPP-MeOT2) copolymers. (b) Simplified schematic relating energy levels of active materials, using IPs of netural polymers, to the standard electrode potentials for the ORR. η represents the free energy difference between reactants and products (η_1 for the H_2O_2 pathway and η_2 for the H_2O_2 pathway). (c) Stability pulsing experiment by alternating the gate potentials between $V_G = 0\ V$ and i) $V_G = -0.5\ V$, ii) $V_G = -0.6\ V$, or iii) $V_G = -0.7\ V$ with pulse duration $2\ s$. Adapted with permission.[145] Copyright 2020 John Wiley and Sons.

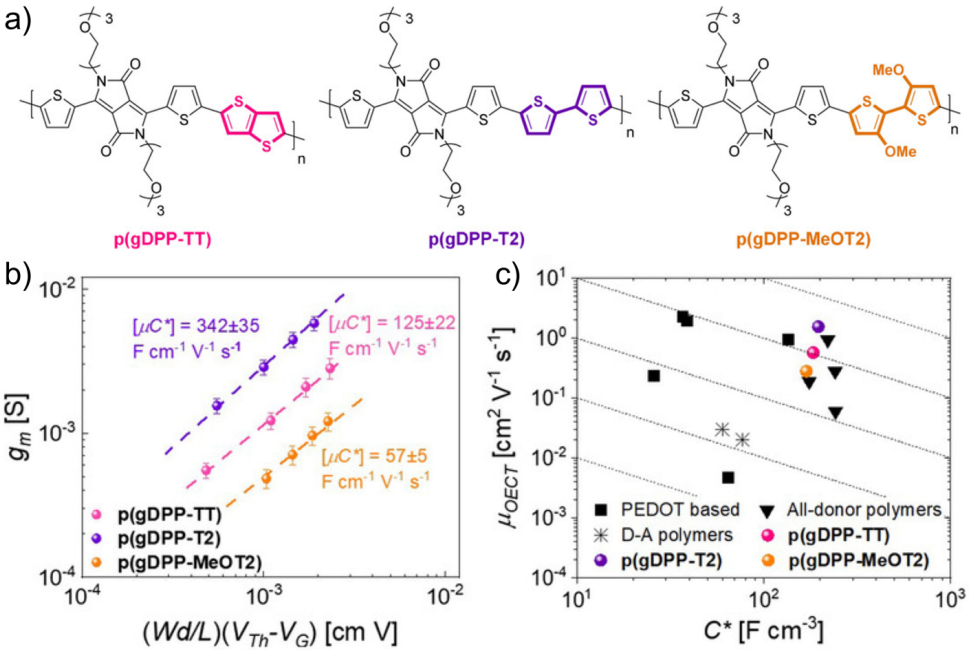

Fig. 16 (a) Chemical structures of p(gDPP-TT), p(gDPP-T2), and p(gDPP-MeOT2) copolymers. (b) Plot of transconductance vs. channel geometry and operating parameters with annotated μC^* figures of merit. (c) Comparison of steady-state performance of the polymer series against other p-type OECT channel materials. Adapted with permission.[148] Copyright 2020 John Wiley and Sons.

with systematically varied glycol- and alkyl-chain functionalized monomer ratios was investigated to determine the optimal balance between appropriate swelling in aqueous solution and efficient electron mobility.[153] Starting with the copolymer structure of poly([N,N'-bis(2-octyldodecyl)-naphthalene-1,4,5,8-bis(dicarboximide)-2,6-diyl]-*alt*-5,5'-(2,2'-bithiophene)) (P(NDI2OD-T2))[157] incorporating branched, hydrophobic 2-octyldodecyl (2OD) side-chains, random terpolymers were synthesized using a methyl end-capped heptakis(ethylene glycol) functionalized NDI derivative (g7-NDI-Br2) to afford a polymer series with 100%, 90%, 75%, 50%. 25%, 10%, and 0% glycolated monomer incorporation (P-100, P-90, P-75, P-50, P-25, P-10, and P-0 = P(NDI2OD-T2).

Dramatic differences were observed in ion penetration into the bulk during electrochemical redox reactions, as observed through shifts in the the reduction onset from 1.12 V for 0% glycol fraction (P-0) to 0.24 V for 100% glycol fraction (P-100). This shift in the reduction potential likely originates from the difference in ion penetration into the bulk during electrochemical redox reactions. Polymers with glycolated monomer percentages $< 25\%$ operated as OFETs and showed low degree of swelling ($< 10\%$) precluding their use within OECTs. Significant degrees of swelling 12% (P-75), 42% (P-90), and 102% (P-100) and lowered hysteresis during electrochemical redox reactions were observed at $> 75\%$ glycolated monomer incorporation, enabling efficient operation within OECTs. Of the active materials that operated within an OECT, P-90 displayed the highest volumetric capacitance C^* ($198.2\ F\ cm^{-3}$), electron mobility μ_{el} ($2.38 \times 10^{-4}\ cm^2\ V^{-1}\ s^{-1}$), and normalized transconductance g_m ($0.210\ S\ cm^{-1}$), highlighting the role of both backbone composition and side-chain engineering (hydrophobic vs. hydrophilic ratio) in the design of novel n-type OECT materials.

Recent efforts have focused on further improving the performance of P-90 through solvent engineering to improve ion penetration,[155] as well as n-doping to increase electron mobility (μ_{el}).[154] By admixing Lewis basic n-dopant tetra-n-butylammonium fluoride (TBAF) with P-90, improvements in electron mobility, ion uptake and storage, and favorable microstructure to support facile ion penetration and migration can be realised (Figure 17).[154] When doping P-90 with TBAF at various concentrations, the highest -performing OECT was produced with 40 $mol\%$ ($g_{m,max} = 10.5\ \mu\ S$), demonstrating an order of magnitude enhancement in the maximum transconductance and similar performance to p(gNDI-gT2) (Figure 17c).

The peak μ was achieved at 40 $mol\%$ ($18.4 \times 10^{-5}\ cm^2\ V^{-1}\ s^{-1}$) which was attributed to trap filling and at high doping concentrations ($60 - 80\ mol\%$) drops in μ were observed which was assiciated with lattice disturbances. Molecular doping was verified using electron paramagnetic resonance (EPR) spectroscopy, which delocalized electrons present in the high-performing P-90:TBAF (40 $mol\%$) film that were not present in pristine P-90. Atomic force microscopy (AFM) also suggested TBAF acted as a morphological additive which synergistically smoothed surfaces features and led to a more dense active layer (reduction in film thickness from 160 nm at 0 $mol\%$ to 116 nm at 40 $mol\%$) without disrupting molecular ordering.

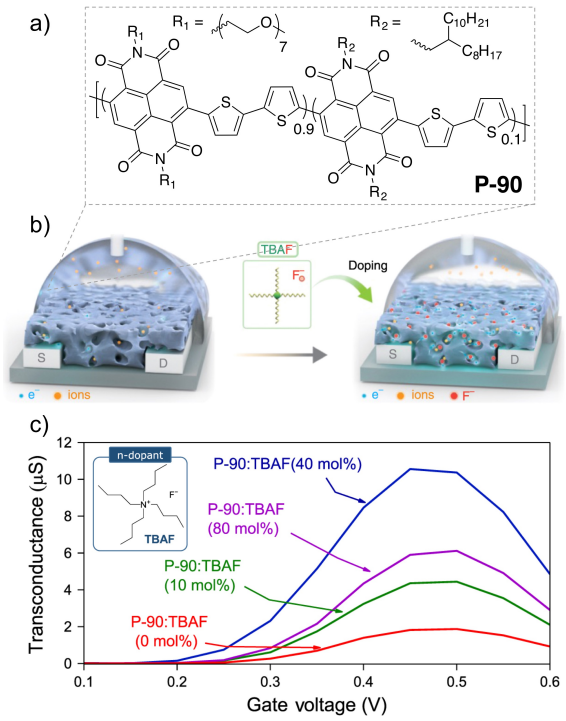

Fig. 17 (a) Chemical structure of P-90. (b) OECT configuration and graphical illustration representing TBAF doping mechanisms in P-90. (c) Transconductance of P-90 OECT containing 0, 10, 40, and 80 molar percentage (mol%) TBAF. Maximum transconductance is taken at $V_G \approx 0.5\ V$ and $V_D \approx 0.6\ V$.[154]

The increased performance of P-90 as well as enhanced shelf-life and operational stability through molecular doping suggests a broader range of active materials may be suitable for n-type OECT devices.

While the high-performance of P-90 has recently afforded several n-type OECT-based sensors,[29,158,159] there are fundamental limitations in the design of P-90 which manifest from the D-A alternating copolymer architecture. Rotational torsion (interannular) between monomers gives rise to conformational disorder, limiting charge carrier mobilities. In addition, D-A systems localize the distribution of LUMO frontier molecular orbitals which hinders charge hopping, carrier mobilities, and stability. Taken together, reducing D-A character while increasing backbone planarity would be advantageous.[149] OECTs utilizing a rigid and planar ladder-type polymer, poly(benzobisimidazobenzophenanthroline (BBL), demonstrated significant enhancements in conductivity ($\sim 1000\times$) and channel-area-normalized g_m ($\sim 2.5\times$) compared to high performing NDI-based OECTs.[160] The lack of side-chains in BBL lead to a high volumetric capacitance over 900 $F\ cm^{-3}$ at an offset voltage of $-0.5\ V$. The high conductivity and electron affinity allowed OECT operation at high currents in water. However, the lack of side-chains in BBL also limited the diffusion of ions resulting in a slow response speed. Recently, another n-type rigid backbone design based on fused electron-deficient aryl lactam rings with oligoether side-chains was reported.[161] The polymer backbone featured a fully conformationally locked structure, which pro-

moted coplanarity and delocalized molecular orbitals, while the side-chains promoted processability and ion diffusion. OECTs incorporating these polymers demonstrated a maximum dimensionally normalized transconductance of 0.212 $S\ cm^{-1}$ and a $\mu\ C^*$ of 0.662 $\pm 0.113\ F\ cm^{-1}V^{-1}s^{-1}$, comparable to BBL and other high-performance materials. Similarly, fused polymer structures with multiple sites for side-chain modification may allow for tunable high-performance n-type materials for OECTs. Other attempts to improve upon common n-type materials through side-chain engineering are discussed in Section 5.1.5

5.1.5 Side-chain Engineering.

Since the original demonstration of oligoether side-chains facilitating hydration and ion penetration in an active material,[132] the highest reported transconductance values and ON/OFF ratios have been obtained with neutral glycolated conjugated polymers.[53] The electron rich alkyl-aryl-ether linkage lowers the IP, stabilizes the oxidized (polaron or bipolaron) states, and leads to favorable intramolecular noncovalent $S-O$ interactions within thiophene based materials.[107] While side-chain engineering has been extensively studied in the OFET and OPV communities,[162] only recent works have started to elucidate the impact of oligoether side-chain engineering in active materials for OECTs.[105,130,131,153,163–165] Recent work has identified a trade-off between hydrating the channel for ion conduction and maintaining good charge transport, both of which are strongly correlated to the morphology of the polymer. For example, a glycolated analogue of P3HT, poly(3-{[2-(2-methoxyethoxy)ethoxy]methyl}thiophene-2,5-diyl) (P3MEEMT) demonstrated faster anion injection kinetics compared to P3HT, which were largely independent of anion identity.[164] It was shown that the crystal lattice of P3MEEMT readily expanded in solution to allow ions to move throughout the material, and the degree of crystallinity had a dramatic effect on how hydration impacted the connectivity of crystalline domains within the film, and therefore OECT mobility. Increasing the crystallinity of P3MEEMT demonstrated a decrease in OECT mobility as hydration disrupted links between crystalline domains, therefore complicating the design of active materials for OECTs.

Investigations of the influence of water on OECTs have suggested that swelling can lead to structural changes due to water accumulation that impairs hole mobility.[136] These phenomena were further investigated using three homopolymers (P3MEET, P3MEEMT, and P3MEEET) which varied by different links between the backbone and diethylene glycol side-chains (Figure 18a).[165] While only the linkage between the oligoether side-chain and the backbone differ, the structure formation, swelling, volumetric capacitance, and charge carrier mobility dramatically differed between the three polymers. With increasing length of the alkyl spacer between the first oxygen of the side-chain and the backbone, molecular order increased with P3MEEMT demonstrating the highest crystallinity of 58%. When operating OECTs with each of the active materials (Figure 18b), P3MEEET demonstrated the best performance with the highest figure of merit ($\mu C^* = 11.5\ F\ cm^{-1}\ V^{-1}\ s^{-1}$) which was mainly attributed to the high volumetric capacitance ($C^* = 242 \pm 17\ F\ cm^{-3}$) (Figure 18c) further correlated to 12-fold increase mass uptake in the oxidized state. While the μ_{OECT} values of P3MEEMT and P3MEEET were almost identical (0.06 and 0.05 $cm^2\ V^{-1}\ s^{-1}$ Figure 18d), the increased spacer length of P3MEEET allowed better accessibility of the diethylene glycol side-chains and thus enhanced ion transport and ordering, increasing the overall performance of the active material.

Recent work has also focused on side-chain engineering through the systematic modification of p(g2T-TT) and p(g2T-T) to balance ionic and electronic conduction (Figure 12b).[105,130] A series of p(2T-TT) analogs with varying amounts of glycolated side chains were used to tune hydrophilicity. Linear alkyl side-chains were exchanged from the fully alkylated co-polymer poly(2-(3,3'-bis(tetradecyloxy)-[2,2'=bithiophene]-5-yl)thieno[3,2-*b*]thiophene) (p(a2T-TT)) to the fully glycolated copolymer p(g2T-TT), with "g-50%" and "g-75%" random terpolymers with glycol:alkyl monomer ratios of 50:50 and 75:25, respectively, and "2g" a copolymer analogue of p(g2T-TT) incorporating longer hexakis glycol side-chains.[105] Each of the glycolated copolymers demonstrated dramatic improvements in transconductance compared to p(a2T-TT) due to enhancements in swelling and therefore ion motion,[132] however polymer "2g" showed decreased performance compared to p(g2T-TT) even with longer oligoether side-chains. As suggested in previous studies,[136,164] excessive hydration reduces charging ability and hole mobility through the separation of crystalline regions. During doping, more mass was loaded into the "2g" film compared to p(g2T-TT) (100% and 86% swelling, respectively), while the transconductance, μ_{OECT}, and switching speed decreased.

Similarly, side-chain engineering has been used with p(g2T-T)-based systems to highlight that increased swelling is not always beneficial for OECT performance.[130] A series of glycolated polythiophenes with oligoether side-chain length varying from two to six repeat units exemplifies this balance between hydrophilicity and device performance (Figure 19a). Of the series, p(g6T2-T) was the only polymer that was unsuitable for operation in an OECT due to low stability brought on by significant swelling, delamination, and dispersion upon cycling. At lower chain lengths p(g2T2-T) exhibited a reduced capability to store electronic charges due to insolubility and lack of permeability to ions, and had a mobility that was too low to be determined accurately. Of the remaining two polymers, p(g3T2-T) gave the highest C^* of $211 \pm 18\ F\ cm^{-3}$ as longer side-chain lengths did not contribute to additional stabilization and decreased the proportion of electroactive mass within the material (p(g4T2-T); $C^* = 192 \pm 10\ F\ cm^{-3}$). A preferential edge-on rather than face-on orientation, and a more rigid polymer backbone of p(g3T2-T) compared to p(g4T2-T) also led to a 3-fold higher charge carrier mobility. Taken together p(g3T2-T) demonstrated the best performance with $g_m = 3.03 \pm 0.21\ mS$, and $\mu C^* = 135 \pm 9\ F\ cm^{-1}\ V^{-1}\ s^{-1}$ (Figure 19b), through the careful optimization of side-chain length.

Side-chain engineering has also been utilized to increase active material performance through redistributing oligoether chains within a polymer repeat unit, rather than through simple lengthening.[131] A series of polymers were derived from p(gT2), a ho-

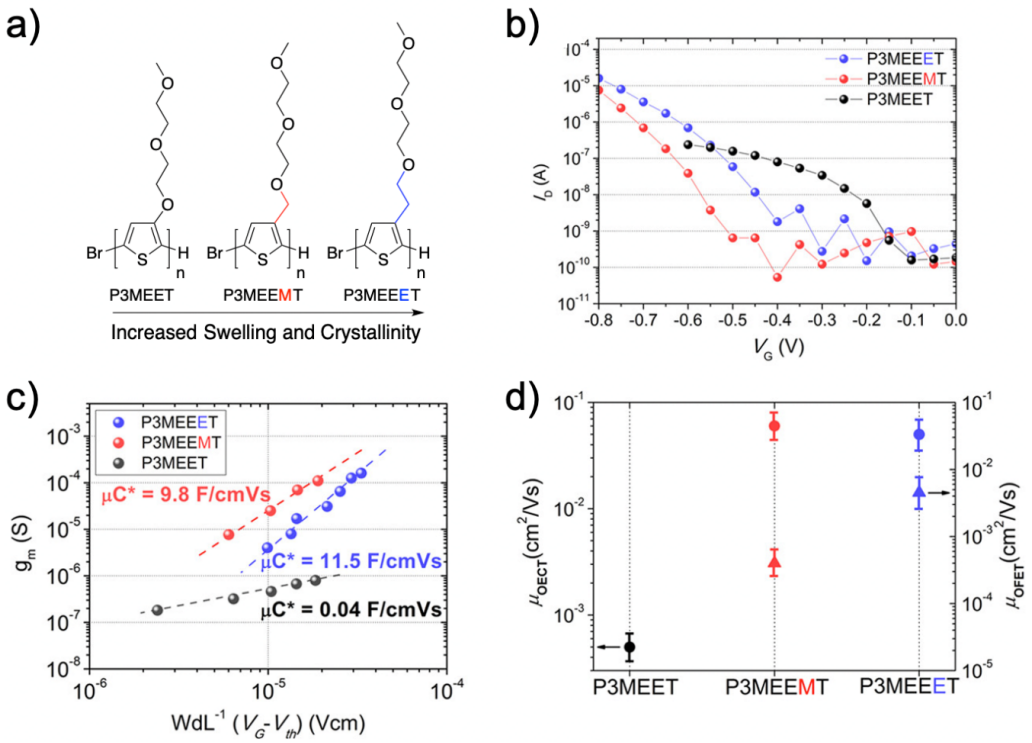

Fig. 18 (a) Chemical structures of P3MEET, P3MEEMT, and P3MEEET homopolymers. (b) Transfer curve of each polymer. $V_D = -0.6\ V$ for P3MEET and $V_D = -0.8\ V$ for P3MEEMT and P3MEEET. (c) Transconductance vs. channel geometry and operation parameters for each polymer. (d) OECT hole mobility extracted in the hydrated state compared to the bulk hole mobility estimated from OFETs. Adapted with permission.[165] Copyright © 2020 American Chemical Society.

mopolymer with triethylene glycol chains,[166] where the ethylene glycol chain length on one structural unit is decreased by one repeat unit and increased on the successive structural unit, affording the same polymer backbone with redistributed side chains (Figure 20a).[131] Four polymers were studied, where an average of three ethylene glycol units per thiophene structural unit was maintained. When operated within OECT configurations, side-chain redistribution increased polymer performance with p(g2T2-g4T2) and p(g1T2-g5T2) displaying extraordinary performance compared to other OECT channel material to date ($\mu C^* = 522\ F\ cm^{-1}\ V^{-1}\ s^{-1}$ and 496 $F\ cm^{-1}\ V^{-1}\ s^{-1}$, respectively). Homopolymer p(g3T2) demonstrated the most active swelling (249%), however, this was not directly proportiona to additional anion uptake and redistributing side chains decreased swelling in p(g2T2-g4T2) (168%) while increasing C^* to $187 \pm 8\ F\ cm^{-3}$ (Figure 20b). Polymers with the least swelling had the highest mobility in line with previous studies.[136] Side-chain engineering provided an alternative route to controlling the polymers ability to take up and stabilize water molecules in the doped state.

Many of the different strategies outlined for side-chain engineering of oligoether groups in p-type systems (length , distribution, and distance from the backbone) have recently been adopted for n-type materials.[153,166,167] We previously discussed the systematic variation and optimization of such side-chains in NDI-T2 based polymers through statistical copolymerization (see Section 5.1.4), where P-90 displayed the finest balance between swelling and conductivity compared to the other materials investigated.[153] While the statistical or random incorporation of functional monomers through copolymerization (backbone engineering) can provide insight into the effects of side-chains (side-chain engineering), this method is imperfect due to batch-to-batch variations in monomer loading and distribution within the polymer. An alternative and more controlled method to systematically tune ratios of hydrophilic oligoether and hydrophobic alkyl side-chains is through the use of hybrid alkyl-glycol side-chains.[163,165] For aqueous-based OECTs with p-type materials, it has been observed that placing a hydrophobic alkyl unit adjacent to the backbone improves long-range ordering and charge carrier mobility.

Recently a series of NDI-T2 polymers with hybrid alkyl-glycol chains with either a propyl (p(C3-gNDI-gT2)) or a hexyl (p(C6-gNDI-gT2)) spacer were synthesized by an alternating copolymerization, providing a controlled series to investigate the effect of alkyl spacers on swelling and stability in n-type systems.[167] As the fraction of hydrophilic side-chain was increased, passive swelling decreased from p(gNDI-gT2) (44%) to p(C6-gNDI-gT2) (13%); the same trend was observed for active swelling. While C^* dramatically decreases upon the introduction of alkyl spacers, the corresponding increase in the OECT electron mobility imparted a higher μC^* for both p(C3-gNDI-gT2) and p(C6-gNDI-gT2) compared to the entirely glycolated control p(gNDI-gT2). OECTs using polymers containing hybrid side-chains also demonstrated superior stability compared to p(gNDI-gT2), which was attributed to the lower extent of swelling during charging. Recently a sim-

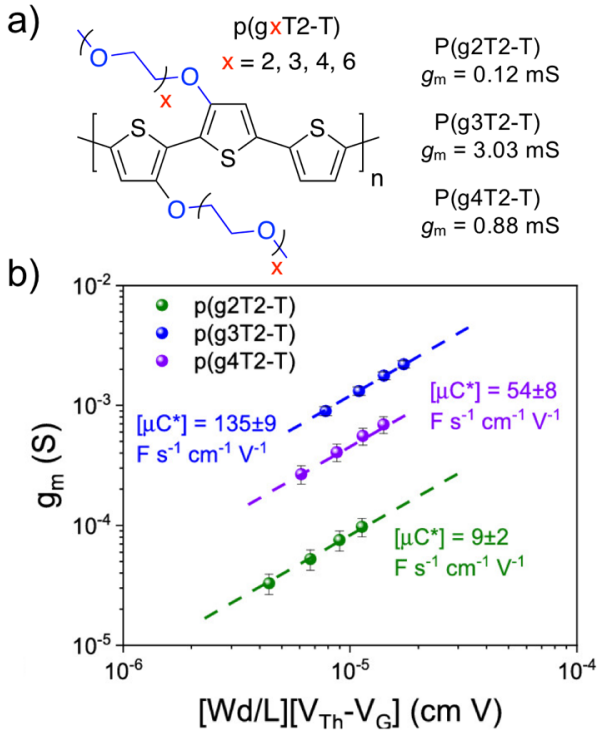

Fig. 19 (a) Chemical structures of p(gxT2-T) polymer series with annotated maximum transconductance. (b) Plot of transconductance vs. channel geometry and operating parameters with annotated μC^* figures of merit. Adapted with permission.[130] Copyright 2020 American Chemical Society.

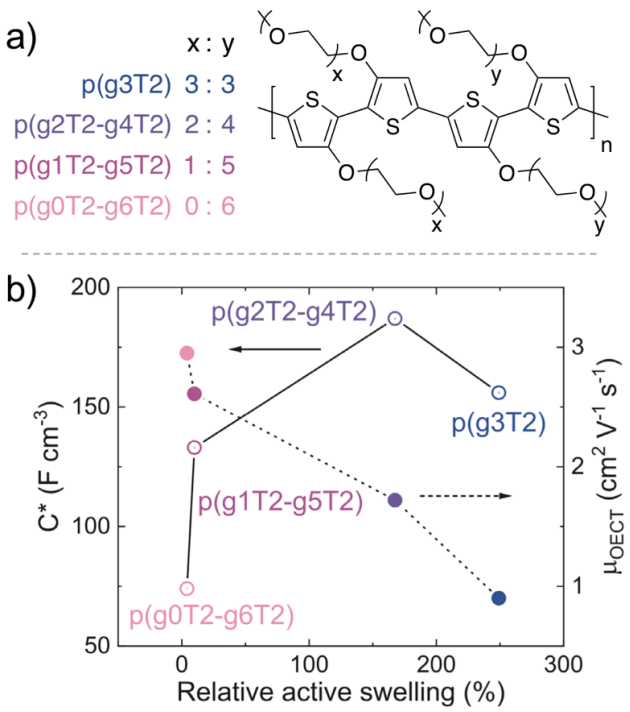

Fig. 20 (a) Chemical structures of polymer series with redistributed ethylene glycol chains. (b) Dependence of C^* and μ_{OECT} on the active swelling for each polymer.[131]

ilar study adopted the same hybrid side-chain approach in NDI-T2 materials and found an optimal μ at a length of six carbon spacers.[168] Compared to shorter and longer alkyl spacers, the six carbon spacer was hypothesized to provide the highest mobility as a result of optimizing microstructural order. As demonstrated in p-type materials,[163–165] controlling the length of alkyl spacer between the oligoether side-chain and the conjugated backbone may be a useful strategy to control swelling, mobility, and improve the long-term operational stability in n-type materials for OECTs.

While these demonstrations highlight the trade-off between μ and C^* through oligoether-induced material swelling, these soft, hygroscopic side-chains complicate material synthesis, create structural disorder within the backbone, demonstrate a tendency to chelate potentially reactive compounds, and may also lead to sensitivity to humidity.[169] Alternative hydrophilic functionalities that enable ion uptake without excessive volumetric expansion would lead to materials with improved mechanical integrity and stability during cycling. Mixed conduction has been demonstrated in hydroxyl-functionalized PT materials, where increased incorporation of polar side-chains promoted ion flow and oxidation.[170] Recently, a hydroxylated analog of P3HT, poly[3-(6-hydroxy)hexylthiophene] (P3HHT) demonstrated faster anion injection kinetics compared to P3HT and substantially reduced swelling compared to other high-performance glycolated conjugated polymers.[171] Passive swelling of P3HHT upon exposure to the aqueous electrolyte (KCl) was investigated using a quartz crystal microbalance with dissipation monitoring (QCM-D). A small thickness change was calculated for the P3HHT/KCl system (+2.4%) compared to that of p(g2T-TT)/KCl (+10% to +15%) and PEDOT:PSS (≈ 85%), which was hypothesized to arise from the lower bulk hydrophilicity of P3HHT. Upon injection of ions/electrolyte into the bulk of the polymer films using a bias of 0.6 V (i.e. active swelling), P3HHT only demonstrated a small mass uptake compared with p(g2T-TT), corresponding to thickness expansions of less than +10% and between +75% to +80%, respectively. The low swelling in P3HHT compared to oligoether-containing materials was attributed to the lower density of polar sites per repeat unit, which reduced water-polymer interactions. When incorporated into an OECT, nearly complete de-doping was observed in P3HHT without the need to apply a negative bias, leading to a high ON/OFF ratio (10^4), and an overall figure of merit ($\mu C^* = 35 \pm 2\ F\ cm^{-1}V^{-1}s^{-1}$) slightly below that of PEDOT:PSS ($\mu C^* = 47 \pm 2\ F\ cm^{-1}V^{-1}s^{-1}$). Hydroxyl-functionalization had little effect on molecular packing and charge transport while avoiding challenging synthetic protocols required for glycolated materials. This chemistry may be an attractive alternative to the sulfonate and oligoether functionalities exclusively used in high-performance materials for OECTs.

5.1.6 Future Directions.

While the introduction of PEDOT:PSS has enabled the widespread development, understanding, and application of OECTs; the highly complex structure, lack of synthetic modularity, extensive processing requirements, and limitation to p-type depletion mode of operation have stunted growth within the field. Recent ad-

vancements in active material design have largely been realized through backbone and side-chain engineering (Table 1). These studies have resulted in materials that outperform PEDOT:PSS and enabled structure-property relationships that offer improved insight into the design of next-generation active materials. PEDOT:PSS is still the most common active material out of convenience, as high-performance glycolated active materials lack accessibility on account of synthetic challenges associated with multi-step monomer synthesis and the transition-metal mediated step-growth polymerization procedures. Recently, advances in synthetic techniques such as direct(hetero)arylation polymerization (DHAP) have been used to simplify access to channel materials,[172,173] however polymer functionalization with hydrophilic side-chains represents the limiting factor. A potential solution to achieve polymer functionalization and efficient side-chain engineering may be through post-polymerization modification or high-yielding chemistries,[174] tools which have only been utilized for biofunctionalization in OECTs.[56,175] The simplified and facile glycolation of high mobility D-A polymers from the OFET and OPV communities is expected to further boost OECT performance. We also expect advances to be made in the development of n-type materials through both backbone and side-chain engineering, leading to exciting opportunities for complementary circuits and performance rivaling p-type materials. Future avenues to advance OECTs through material design will include controlling structure phase transitions,[176,177] material toughening,[178] deformability,[111] and degradability,[179,180] among others.

5.2 Gate Materials

Being an essential component of electrochemical gating,[181] the geometry and material of the electrochemical gate have a significant role in determining the behavior of OECTs. The potential applied at the gate drives the ionic flux for electrochemical doping/dedoping of the organic polymer due to differences in potential throughout the channel and electrolyte.

The ionic circuit displayed in Figure 2 of the Bernards and Malliaras model neglects any voltage drop across the gate/electrolyte interface, i.e. it is assumed that the volumetric capacitance of the channel dominates the device operation. However, this simplification doesn't fully describe the system as a significant fraction of applied potential drops at the gate electrode as well. The fraction of applied potential that drops at the gate was shown to depend on the geometry of gate, material of gate, composition of an electrolyte and also the separation from channel.[182–184]

Different gate electrodes can be categorized into polarizable and non-polarizable ones. In perfectly polarizable electrodes, no actual charge is transferred at the electrode/electrolyte interface. The current across the interface is a displacement current and the electrode behaves as capacitor. Platinum and gold are nearly perfect polarizable electrodes with relatively large charge separation at the electrode-electrolyte boundary, making the interface electrically equivalent to a capacitor. For polarizable electrodes, the surface area determines the magnitude of the double layer capacitance and hence the device performance. For example, activated carbon known to provide a large surface area was used to increase the current modulation of OECTs.[185]

In non-polarizable electrodes, charge is transferred across the electrode-electrolyte interface, effectively reducing the voltage drop across the gate/electrolyte interface. A simplified ionic circuit as proposed by Lin et al.[37] can be assumed to describe OECTs as illustrated in Figure 21a . Ag and Ag/AgCl electrodes are examples and are often used to record small signals. Ag/AgCl is preferable to metallic silver because of its stability and lower electric noise.[183] In contrast to polarizable electrodes, the surface area of the gate electrode was found to not affect the performance significantly in case of these materials.[186]

The role of gate materials on OECTs was studied in detail by Tarabell et al.[186] using Au and Pt gates. Their halide electrolyte based OECTs are shown to work in different regimes depending on the choice of gate material. OECTs with polarizable gates such as Pt operate in a capacitive regime showing a smaller current modulation and a small steady state gate current. Changing the gate from Pt to a non-polarizable material such as Ag, the OECTs are working in a Faradaic regime with relatively large current modulation and gate-voltage dependent steady state gate currents.

Often, the gate electrode is modified by nano-particles (eg. Pt-nanoparticles[187]) or other nano-materials (eg. graphene, rGO etc.[35,187]) to improve their surface to volume ratio and to improve sensitivity to particular analytes. Furthermore, crosslinked enzymes[35,182] are often used to trigger a targeted reaction at the gate, and bio-compatible polymers (chitosan or Nafion[187]) are used to improve the detection limit and sensitivity of OECT based sensors. Chitosan and Nafion can improve the immobilization of enzymes on the gate electrode and enhance the selectivity of the device by allowing only certain analytes to pass through and reach the gate or immobilized catalyst. Similar, a variation in surface engineering conditions to prepare Nitrogen/oxygen-codoped carbon cloths (NOCCs) gate electrodes, enabled highly sensitive and selective ascorbic acid (AA) and dopamine (DA) sensors.[188]

Polymeric gates are used in some cases, in particular when OECTs are printed.[189] PEDOT:PSS is often used not only as active channel material, but to form the gate as well[185,190,191]. However, it has been reported that the gate area has to be large compared to the channel to provide for a sufficient control of the drain current[189].

In addition to the particular material used for the gate, OECT performance depends largely on the geometry of gate and also the separation from the channel.[192,193] For example, the response of H_2O_2 sensors based on PEDOT:PSS electrochemical transistors can be tuned by varying the ratio between the area of the gate electrode and the channel. Devices with small gates showed a lower background signal and higher sensitivity. The ON/OFF ratio increases substantially with a smaller gap between gate and source-drain area.[193]

Table 1 OECT Active Materials Performance Comparison to PEDOT

Material/Formulation	$C^*(F\ cm^{-3})$	$\mu_{OECT}\ (cm^2\ V^{-1}s^{-1})$	$[\mu_{OECT}][C^*]\ (F\ cm^{-1}V^{-1}s^{-1})^{\dagger}$	$[\mu_{OECT}C^*]\ (F\ cm^{-1}V^{-1}s^{-1})^{\ddagger}$	ref
p-type: Operation in Aqueous (Cl^-) Electrolyte					
p(g2T2-g4T2)	187±8	1.72±0.31	322±60	522$^{\parallel}$	[131]
p(gDPP-T2)	196	1.55±0.17	304±33	342±35	[148]
p(g2T-TT)	241±94	0.94±0.25	227±107	261±29	[53]
p(g2T-T)	220±30	0.28±0.1	62±24	167±65	[53]
PTDPP-DT	123	1.1±0.5	135±62	149±61	[147]
p(g3T2-T)	211±18	0.16±0.01	34±3.6	135±9	[130]
p(gDPP-TT)	184	0.57±0.09	105±16.6	125±22	[148]
PEDOT:TOS [VPP]	136±50	0.93±0.72	126±108	72±14	[53]
p(gDPP-MeOT2)	169	0.28±0.04	47.3±6.8	57±5	[148]
P3MEEMT	175	-	-	49.1±5.2	[164]
PEDOT:PSS + EG	39±3	1.9±1.3	75±51	47±6	[53]
P3HHT	-	0.04±0.01	-	35±2	[171]
p(gBDT-g2T)	77±23	0.018±0.006	1.4±0.6	4.8±0.7	[129]
p(gPyDPP-MeOT2)	60	0.030±0.007	1.8±0.4	-	[145]
$PTHS^-TMA^+$-co-P3HT	100±7	0.017±0.0036	1.7±0.4	-	[125]
n-type: Operation in Aqueous (Na^+) Electrolyte					
p(NDI-C6-T2)	272	0.00474±0.000431	1.29±0.117	1.29±0.117	[168]
PgNaN	100±6	0.00650±0.00101	0.650±0.06	0.662±0.113	[161]
BBL	930±40	0.0007	0.651±0.94	∼0.6	[160]
p(NDI-C4-T2)	158	0.00190±0.00000188	0.3±0.0003	0.30±0.0003	[168]
p(gNDI-g2T)	397	0.00031±0.00009	0.12±0.04	0.18±0.01	[53]
p(C6-gNDI-gT2)	59	0.00063	0.04	0.16	[167]
P90	198.2	0.000238	0.048	∼0.06	[153]

† Calculated product from independently derived μ_{OECT} and C^* values.
‡ Average values calculated across several channels. Calculated from the slope of g_m as a function of $(Wd/L)(V_{Th}-V_G)$.
‖ Calculated from the highest performing channel from the slope of g_m as a function of $(Wd/L)(V_{Th}-V_G)$.

5.3 Electrolyte

The choice of possible electrolytes is wide. The electrolyte can be water based, based on room temperature ionic liquids (RTIL), or based on more complex mixtures, yielding a wide range of consistencies from liquid solutions to rubberlike films including hydrogels and cross-linked-solid electrolyte. Whenever water based solutions are preferred, sodium chloride NaCl, potassium chloride KCl and variations of phosphate buffered solution (PBS) are commonly used.[24] Aqueous electrolytes usually lead to a high transconductance, however sometimes at the expense of a lower on/off ratio.

RTILs are another class of versatile but water free electrolytes, which extend the operational window, i.e. can be operated at gate voltages up to or even beyond 1V, which often results in a larger on/off ratio. Though many electrolytes were proposed, commonly used RTILs are 1-ethyl-3-methylimidazolium ethyl sulfate $[E_2mIm][EtSO_4]$? and (1-ethyl-3-methylimidazolium bis(trifluoromethylsulfony1)imide [EMIM][TFSI], BASF SE).[194] These RTILs can be used on their own or in combination with water based salt solutions like NaCl. They are often cross-linked after addition of other components to form solid or gel-type electrolytes.

Gelatin, a semisolid electrolyte, is one of the most widely used natural, thermo-responsive, and protein-based hydrogels that shows excellent biodegradability, biocompatibility, and nontoxicity that is even injectable.[195,196] Patterned gelatin hydrogels can easily be formed by drop-casting on a sacrificial mask film. Casting of so prepared hydrogel on pre-patterned polymer channels was used to realize logic circuits[197] or even pressure sensors.[45] An ion-conducting poly(vinyl alcohol) PVA hydrogel forming a quasi-solid-state polymer electrolyte[23] was shown to be a good electrolyte for bendable and stretchable devices that also increase speed, stability, and provides a self-healing mechanism of cracks developed in Triton X-100 (a nonionic surfactant) mixed PEDOT:PSS channel.

Recently, novel ionic liquid based liquid-crystalline electroactive elastomers were developed, which allows to control the orientation of the monomers and was used to prepare substrate free elastomer based OECTs.[198,199] The use of solid polymer electrolytes leads to all-solid-state OECTs.[200] For wearable sensor technology, that sense analytes in sweat, sweat itself can serve as an electrolyte[15,201] and similarly blood can as well be used as functional component of transistors in implantable devices.[202]

The choice of electrolyte also influences the behavior of OECTs and their targeted use. Both, the concentration and composition are equally important, which was confirmed for a broader range of cations (Li^+, Na^+, Cs^+, Rb^+, K^+, Ca^{2+}) where a direct dependence of impedance of OECTs on the concentration and the nature of these electrolytic cations is reported.[203] The device is found to be more sensitive to large size/mass of cations at low frequencies, while it is more sensitive to the valency and the ionic conductivity at high frequencies. This opens the possibility to selectively detect cations present in the electrolyte by using a single device without specific chemical functionalization.

The ON/OFF ratio of OECTs depends largely on the choice of electrolyte used for gating.[24,84,204] Higher ON/OFF ratios are achieved when cetyltrimethyl ammonium bromide (CTAB) is used as the electrolyte instead of NaCl,[204] which can be improved fur-

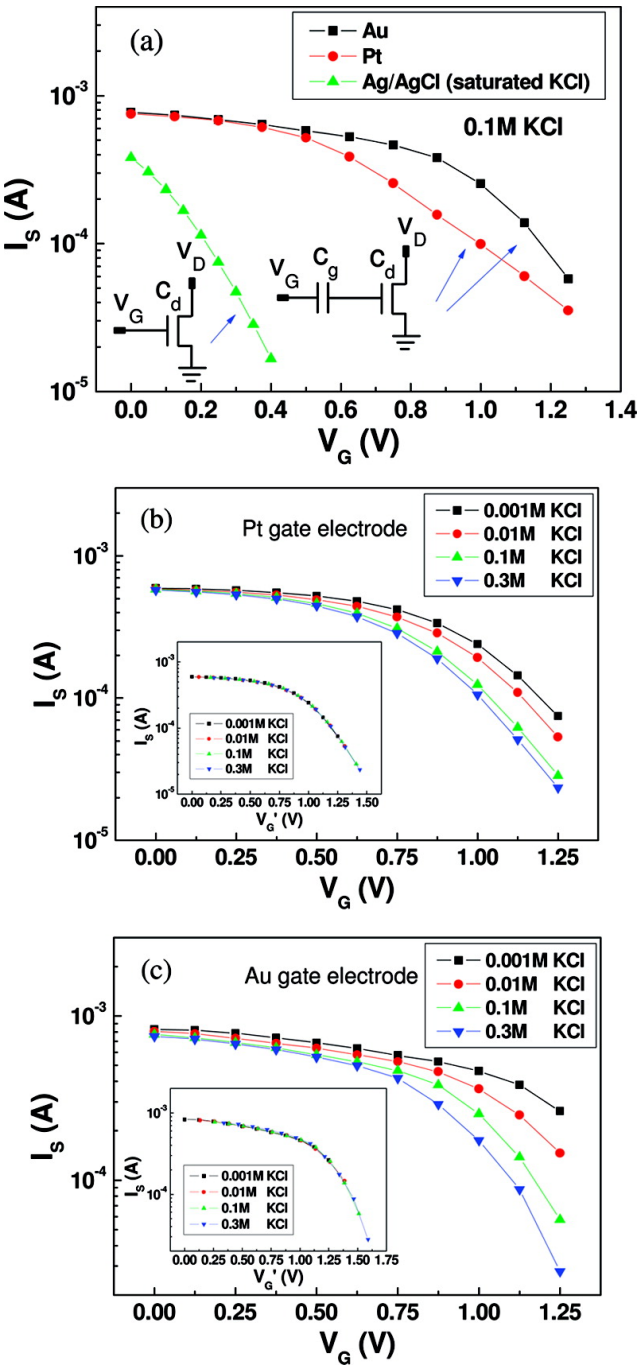

Fig. 21 (a) Transfer characteristics of OECTs measured in *KCl* solutions with different gate electrodes. (b,c) Transfer characteristics of OECTs with Pt and Au gate electrodes, respectively. The OECTs are measured in *KCl* solutions with different concentrations. Insets show transfer characteristics of the OECTs where the curves are scaled in x-axis to yield a universal curve. $V_D = -0.1\ V$ is used in all cases. Copyright © 2010 American Chemical Society.[37]

ther when RTIL mixed with a solution of smaller ions is used.[24] It is claimed that the cation of the RTIL C_2mIm^+ alone is too large to effectively de-dope the organic semiconductor PEDOT:PSS. It is also shown that the use of crosslinked electrolyte improves temporal stability of OECTs.[24]

The concentration of ions inside an electrolyte makes a notable difference. Sometimes, its effect depends on the channel material and the operation mode as well. For PEDOT:PSS polymer based systems, which are used in depletion mode devices, hydration is always beneficial.[52,205] But, for p(g2T-TT) based p-type accumulation mode transistors, less injection of water into the channel results in higher transconductance and faster switching speeds.[136] This observation was explained by the fact that concentrated electrolytes minimize the volumetric expansion of the polymer films enhancing mobility of electronic charge carriers. The optimization of the concentration depends on the active material used for highly efficient ion-to-electron transduction devices. Also, the transfer curves of the OECTs shift to lower gate voltage horizontally with the increase of the concentration of cations in the electrolyte (cf. Figure 21b-c) implying their good ion-sensitivity.[37]

5.4 Source/Drain Electrode

Although the source/drain electrode materials are known to have a strong influence on organic electronic devices, the effects of electrode materials on OECTs only recently moved into the focus of research. Gold is still the most commonly used source/drain electrode in OECT[28,48,94]. The Fermi-level of the gold almost matches the HOMO level of most p-type organic materials for e.g. PEDOT:PSS, but a contact resistance remains which influences the device performance[55,81,93,94], as discussed in Section 4.1.

Ersman et al. studied the improvement device characteristics caused by inserting a carbon conductor layer on top of PEDOT:PSS at the drain electrode[206]. This carbon electrode helps to reduce the time needed to switch the device from off-to-on by suppressing the effect of a reduction front extending into the PEDOT:PSS contact. Three devices were compared. The first used PEDOT:PSS based electrodes, in the second one carbon electrodes were inserted at the source/drain electrode, and in the third the carbon conductor was inserted at the drain electrode only. The switching time from on-to-off were found to be comparable but switching from off-to-on was faster for the device with carbon electrodes.

Overall, microscopic models are needed to understand charge injection in the presence of large ion concentration at the source and drain electrodes in more detail, and to guide materials selection for better contacts. The 2D drift diffusion model by Paudel et al.[84] demonstrate the effects of contact resistance on the maximum transconductance, but still treats the injection mechanism in a highly simplified manner.

Not only is energy alignment and contact resistance of OECTs influenced by the contact materials, but the choice of material determines the flexibility to the device as well. PEDOT:PSS itself as the source-drain electrode in OECT was used by Bihar et al.[207]. They realized flexible alcohol sensing organic electrochemical transistor using PEDOT:PSS source-drain electrode

which requires no metal deposition and is made on an inexpensive, disposable, and biodegradable paper support[207].

6 Outlook

After their invention in 1984[106] OECTs have reached a maturity that is sufficient for first applications, most importantly in the form of biosensors or other bio-electronic applications. Vast experimental progress has been made and the performance of OECTs has continuously been pushed further.

However, most of this progress was reached despite an incomplete understanding of the precise working mechanisms of OECTs. Often, a capacitive coupling of the gate on the transistor channel is assumed, which however might not describe the steady-state of the transistors correctly. Two dimensional drift-diffusion models were used to improve OECT device models, but these models face their own shortcomings. Further research is needed to clarify the extent of separation between an ion- and hole conducting phase in the mixed conductor, to study the dependency of the hole mobility on the electric field, ion concentration, and ion concentration, and to understand injection and extraction at the source and drain electrodes in the presence of a high density of ions.

Our incomplete understanding of OECT device physics makes it challenging to find clear design rules for high-performance OECT materials. A compromise between ion and hole mobility, between swelling in solvents and retaining high structural fidelity, and between high transconductance and low off-currents has to be found, but without predictive device models such an optimization has to be pursued by trial and error. Nevertheless, the library of OECT materials is ever growing and trends in the field are emerging, which focus on both backbone and side-chain engineering of the channel material.

Not only have high performance OECTs been demonstrated, but a surprising variety of different functionalities have emerged. Through rational electrolyte selection and gate functionalization, OECTs can be made sensitive to a wide array of analytes. Furthermore, the complex time response of OECTs enables their use as functional elements of neuromorphic circuits. Overall, the wide choice in materials that can be used for the gate, the electrolyte, the organic semiconductor, and even the source/drain electrode presents a huge parameter space that we are only starting to explore, and which will continue to provide new and exciting inventions in the future.

Conflicts of interest

There are no conflicts to declare.

Acknowledgements

B.L., P.R.P. and V.K. acknowledge funding from the National Science Foundation (Grant ECCS 1750011 and ECCS 1709479). J.D.A. and J.T. acknowledge support from the National Science Foundation (OIA 1632825) and Office of Naval Research (Grant Number: N00014-19-1-2687)

Notes and references

1 B. D. Paulsen, K. Tybrandt, E. Stavrinidou and J. Rivnay, *Nature materials*, 2020, **19**, 13–26.

2 J. Rivnay, R. M. Owens and G. G. Malliaras, *Chemistry of Materials*, 2014, **26**, 679–685.

3 P. Tehrani, N. D. Robinson, T. Kugler, T. Remonen, L.-O. Hennerdal, J. Häll, A. Malmström, L. Leenders and M. Berggren, *Smart Materials and Structures*, 2005, **14**, N21.

4 M. Zabihipour, R. Lassnig, J. Strandberg, M. Berggren, S. Fabiano, I. Engquist and P. A. Ersman, *npj Flexible Electronics*, 2020, **4**, 15.

5 P. A. Ersman, D. Westerberg, D. Tu, M. Nilsson, J. Åhlin, A. Eveborn, A. Lagerlöf, D. Nilsson, M. Sandberg, P. Norberg *et al.*, *Flexible and Printed Electronics*, 2017, **2**, 045008.

6 M. Nishinaka, H. Jinno, Y. Jimbo, S. Lee, J. Wang, W. Lee, T. Yokota and T. Someya, *Small Structures*, 2020, **2**, 2000088.

7 M. Afonso, J. Morgado and L. Alcácer, *Journal of Applied Physics*, 2016, **120**, 165502.

8 R. Mannerbro, M. Ranlöf, N. Robinson and R. Forchheimer, *Synthetic metals*, 2008, **158**, 556–560.

9 T. N. Mangoma, S. Yamamoto, G. G. Malliaras and R. Daly, *Advanced Materials Technologies*, 2020, 2000798.

10 D. J. Macaya, M. Nikolou, S. Takamatsu, J. T. Mabeck, R. M. Owens and G. G. Malliaras, *Sensors and Actuators B: Chemical*, 2007, **123**, 374–378.

11 P. C. Hütter, T. Rothländer, G. Scheipl and B. Stadlober, *IEEE Transactions on Electron Devices*, 2015, **62**, 4231–4236.

12 E. Macchia, P. Romele, K. Manoli, M. Ghittorelli, M. Magliulo, Z. M. Kovács-Vajna, F. Torricelli and L. Torsi, *Flexible and Printed Electronics*, 2018, **3**, 034002.

13 J. Kawahara, P. A. Ersman, K. Katoh and M. Berggren, *IEEE transactions on electron devices*, 2013, **60**, 2052–2056.

14 D. Nilsson, T. Kugler, P.-O. Svensson and M. Berggren, *Sensors and Actuators B: Chemical*, 2002, **86**, 193–197.

15 I. Gualandi, M. Marzocchi, A. Achilli, D. Cavedale, A. Bonfiglio and B. Fraboni, *Scientific reports*, 2016, **6**, 33637.

16 X. Qing, Y. Wang, Y. Zhang, X. Ding, W. Zhong, D. Wang, W. Wang, Q. Liu, K. Liu, M. Li *et al.*, *ACS applied materials & interfaces*, 2019, **11**, 13105–13113.

17 A. Yang, Y. Li, C. Yang, Y. Fu, N. Wang, L. Li and F. Yan, *Advanced Materials*, 2018, **30**, 1800051.

18 J. Feng, C. Chen, X. Sun and H. Peng, *Accounts of Materials Research*, 2021, **2**, 138–146.

19 T. Someya, Z. Bao and G. G. Malliaras, *Nature*, 2016, **540**, 379–385.

20 Y. Li, N. Wang, A. Yang, H. Ling and F. Yan, *Advanced Electronic Materials*, 2019, **5**, 1900566.

21 S. Zhang, E. Hubis, G. Tomasello, G. Soliveri, P. Kumar and F. Cicoira, *Chemistry of Materials*, 2017, **29**, 3126–3132.

22 S. Zhang and F. Cicoira, *Advanced Materials*, 2017, **29**, 1703098.

23 J. Ko, X. Wu, A. Surendran, B. T. Muhammad and W. L. Leong, *ACS Applied Materials & Interfaces*, 2020, **12**, 33979–33988.

24 V. Kaphle, S. Liu, C.-M. Keum and B. Lüssem, *physica status solidi (a)*, 2018, **215**, 1800631.

25 S. Y. Yang, F. Cicoira, R. Byrne, F. Benito-Lopez, D. Diamond, R. M. Owens and G. G. Malliaras, *Chemical Communications*, 2010, **46**, 7972–7974.

26 M. J. Donahue, A. Williamson, X. Strakosas, J. T. Friedlein, R. R. McLeod, H. Gleskova and G. G. Malliaras, *Advanced Materials*, 2018, **30**, 1705031.

27 J. Ji, M. Li, Z. Chen, H. Wang, X. Jiang, K. Zhuo, Y. Liu, X. Yang, Z. Gu, S. Sang *et al.*, *Nano Research*, 2019, **12**, 1943–1951.

28 P. Lin, X. Luo, I.-M. Hsing and F. Yan, *Advanced Materials*, 2011, **23**, 4035–4040.

29 A. Koklu, D. Ohayon, S. Wustoni, A. Hama, X. Chen, I. McCulloch and S. Inal, *Sensors and Actuators B: Chemical*, 2021, **329**, 129251.

30 A. M.-D. Wan, S. Inal, T. Williams, K. Wang, P. Leleux, L. Estevez, E. P. Giannelis, C. Fischbach, G. G. Malliaras and D. Gourdon, *Journal of Materials Chemistry B*, 2015, **3**, 5040–5048.

31 S. Inal, A. Hama, M. Ferro, C. Pitsalidis, J. Oziat, D. Iandolo, A.-M. Pappa, M. Hadida, M. Huerta, D. Marchat *et al.*, *Advanced Biosystems*, 2017, **1**, 1700052.

32 D. A. Bernards, D. J. Macaya, M. Nikolou, J. A. DeFranco, S. Takamatsu and G. G. Malliaras, *Journal of Materials Chemistry*, 2008, **18**, 116–120.

33 D. Khodagholy, V. F. Curto, K. J. Fraser, M. Gurfinkel, R. Byrne, D. Diamond, G. G. Malliaras, F. Benito-Lopez and R. M. Owens, *Journal of Materials Chemistry*, 2012, **22**, 4440–4443.

34 D. Nilsson, T. Kugler, P.-O. Svensson and M. Berggren, *Sensors and Actuators B: Chemical*, 2002, **86**, 193–197.

35 C. Liao, M. Zhang, L. Niu, Z. Zheng and F. Yan, *J. Mater. Chem. B*, 2014, **2**, 191.

36 L. Kergoat, B. Piro, D. T. Simon, M.-C. Pham, V. Noël and M. Berggren, *Advanced Materials*, 2014, **26**, 5658–5664.

37 P. Lin, F. Yan and H. L. Chan, *ACS applied materials & interfaces*, 2010, **2**, 1637–1641.

38 L. Chen, J. Wu, F. Yan and H. Ju, *Biosensors and Bioelectronics*, 2021, **175**, 112878.

39 H. Bai, K. Vyshniakova, E. Pavlica, V. M. Rocha Malacco, A. Yiannikouris, T. R. Yerramreddy, S. S. Donkin, R. M. Voyles and R. A. Nawrocki, *IEEE Sensors Letters*, 2020, **4**, 1–4.

40 J. E. Tyrrell, M. G. Boutelle and A. J. Campbell, *Advanced Functional Materials*, 2021, **31**, 2007086.

41 J. Wang, S. Lee, T. Yokota, Y. Jimbo, Y. Wang, M. O. G. Nayeem, M. Nishinaka and T. Someya, *ACS Applied Electronic Materials*, 2020, **2**, 3601–3609.

42 Y. van De Burgt, A. Melianas, S. T. Keene, G. Malliaras and A. Salleo, *Nature Electronics*, 2018, **1**, 386–397.

43 P. Gkoupidenis, N. Schaefer, B. Garlan and G. G. Malliaras, *Advanced Materials*, 2015, **27**, 7176–7180.

44 Y. Yan, Q. Chen, X. Wu, X. Wang, E. Li, Y. Ke, Y. Liu, H. Chen and T. Guo, *ACS Applied Materials & Interfaces*, 2020, **12**, 49915–49925.

45 X. Wang, X. Meng, Y. Zhu, H. Ling, Y. Chen, Z. Li, M. C. Hartel, M. R. Dokmeci, S. Zhang and A. Khademhosseini, *IEEE Electron Device Letters*, 2020, **42**, 46–49.

46 P. Leleux, J. Rivnay, T. Lonjaret, J.-M. Badier, C. Bénar, T. Hervé, P. Chauvel and G. G. Malliaras, *Advanced Healthcare Materials*, 2015, **4**, 142–147.

47 D. Khodagholy, T. Doublet, P. Quilichini, M. Gurfinkel, P. Leleux, A. Ghestem, E. Ismailova, T. Hervé, S. Sanaur, C. Bernard *et al.*, *Nature communications*, 2013, **4**, 1575.

48 G. Dijk, A. L. Rutz and G. G. Malliaras, *Advanced Materials Technologies*, 2020, **5**, 1900662.

49 S. H. Kim, K. Hong, W. Xie, K. H. Lee, S. Zhang, T. P. Lodge and C. D. Frisbie, *Advanced Materials*, 2013, **25**, 1822–1846.

50 C. R. Kagan and P. Andry, *Thin-Film Transistors*, CRC Press, 2003.

51 D. A. Bernards and G. G. Malliaras, *Advanced Functional Materials*, 2007, **17**, 3538–3544.

52 A. Elschner, S. Kirchmeyer, W. Lovenich, U. Merker and K. Reuter, *PEDOT: principles and applications of an intrinsically conductive polymer*, CRC press, 2010.

53 S. Inal, G. G. Malliaras and J. Rivnay, *Nature communications*, 2017, **8**, 1767.

54 J. Rivnay, S. Inal, A. Salleo, R. M. Owens, M. Berggren and G. G. Malliaras, *Nature Reviews Materials*, 2018, **3**, 17086.

55 J. T. Friedlein, R. R. McLeod and J. Rivnay, *Organic Electronics*, 2018, **63**, 398–414.

56 L. Bai, C. G. Elósegui, W. Li, P. Yu, J. Fei and L. Mao, *Frontiers in chemistry*, 2019, **7**, 313.

57 D. Tu and S. Fabiano, *Applied Physics Letters*, 2020, **117**, 080501.

58 A. Spanu, L. Martines and A. Bonfiglio, *LAB ON A CHIP*, 2021, **21**, 795–820.

59 J. T. Friedlein, S. E. Shaheen, G. G. Malliaras and R. R. McLeod, *Advanced Electronic Materials*, 2015, **1**, 1500189.

60 J. Rivnay, P. Leleux, M. Ferro, M. Sessolo, A. Williamson, D. A. Koutsouras, D. Khodagholy, M. Ramuz, X. Strakosas, R. M. Owens, C. Benar, J.-M. Badier, C. Bernard and G. G. Malliaras, *Science Advances*, 2015, **1**, e1400251.

61 V. Prigodin, F. Hsu, Y. Kim, J. Park, O. Waldmann and A. Epstein, *Synthetic metals*, 2005, **153**, 157–160.

62 N. D. Robinson, P.-O. Svensson, D. Nilsson and M. Berggren, *Journal of the Electrochemical Society*, 2006, **153**, H39.

63 W. Shockley, *Proceedings of the IRE*, 1952, **40**, 1365–1376.

64 V. Prigodin, F. Hsu, J. Park, O. Waldmann and A. Epstein, *Physical Review B*, 2008, **78**, 035203.

65 S. V. Novikov, D. H. Dunlap, V. M. Kenkre, P. E. Parris and A. V. Vannikov, *Physical Review Letters*, 1998, **81**, 4472.

66 I. Fishchuk, A. Kadashchuk, J. Genoe, M. Ullah, H. Sitter, T. B. Singh, N. Sariciftci and H. Bässler, *Physical Review B*, 2010, **81**, 045202.

67 R. Coehoorn, W. Pasveer, P. Bobbert and M. Michels, *Physical Review B*, 2005, **72**, 155206.

68 M. Vissenberg and M. Matters, *Physical Review B*, 1998, **57**, 12964.

69 R. Colucci, H. F. de Paula Barbosa, F. Günther, P. Cavassin and G. C. Faria, *Flexible and Printed Electronics*, 2020, **5**, 013001.

70 A. J. Campbell, R. Rawcliffe, A. Guite, J. C. D. Faria, A. Mukherjee, M. A. McLachlan, M. Shkunov and D. D. Bradley, *Advanced Functional Materials*, 2016, **26**, 3720–3729.

71 P. Blom, M. De Jong and M. Van Munster, *Physical Review B*, 1997, **55**, R656.

72 Y. Shen, K. Diest, M. H. Wong, B. R. Hsieh, D. H. Dunlap and G. G. Malliaras, *Physical Review B*, 2003, **68**, 081204.

73 A. J. Bard and L. R. Faulkner, *Electrochemical Methods.*, John Wiley & Sons, New York, 1980.

74 F. Gentile, D. Delmonte, M. Solzi, M. Villani, S. Iannotta, A. Zappettini and N. Coppede, *Organic Electronics*, 2016, **35**, 59–64.

75 J. T. Friedlein, M. J. Donahue, S. E. Shaheen, G. G. Malliaras and R. R. McLeod, *Advanced Materials*, 2016, **28**, 8398–8404.

76 G. C. Faria, D. T. Duong, A. Salleo, C. A. Polyzoidis, S. Logothetidis, J. Rivnay, R. Owens and G. G. Malliaras, *MRS Communications*, 2014, **4**, 189–194.

77 G. C. Faria, D. T. Duong and A. Salleo, *Organic Electronics*, 2017, **45**, 215–221.

78 N. Coppede, M. Villani and F. Gentile, *Scientific Reports*, 2014, **4**, 4297.

79 J. E. B. Randles, *Discussions of The Faraday Society*, 1947, **1**, 11–19.

80 F. Gentile, M. Ferrari and P. Decuzzi, *Annals of Biomedical Engineering*, 2008, **36**, 254–261.

81 A. V. Volkov, K. Wijeratne, E. Mitraka, U. Ail, D. Zhao, K. Tybrandt, J. W. Andreasen, M. Berggren, X. Crispin and I. V. Zozoulenko, *Advanced Functional Materials*, 2017, **27**, 1700329.

82 V. Kaphle, P. R. Paudel, D. Dahal, R. K. Radha Krishnan and B. Lüssem, *Nature communications*, 2020, **11**, 2515.

83 M. Z. Szymański, D. Tu and R. Forchheimer, *IEEE Transactions on Electron Devices*, 2017, **64**, 5114–5120.

84 P. R. Paudel, V. Kaphle, D. Dahal, R. K. Radha Krishnan and B. Lüssem, *Advanced Functional Materials*, 2021, **31**, 2004939.

85 K. Tybrandt, I. V. Zozoulenko and M. Berggren, *Science advances*, 2017, **3**, eaao3659.

86 A. Shirinskaya, G. Horowitz, J. Rivnay, G. G. Malliaras and Y. Bonnassieux, *Biosensors*, 2018, **8**, 103.

87 E. Stavrinidou, P. Leleux, H. Rajaona, M. Fiocchi, S. Sanaur and G. G. Malliaras, *Journal of Applied Physics*, 2013, **113**, 244501.

88 M. S. Kilic, M. Z. Bazant and A. Ajdari, *Physical review E*, 2007, **75**, 021503.

89 R. E. Bank, D. J. Rose and W. Fichtner, *SIAM Journal on Scientific and Statistical Computing*, 1983, **4**, 416–435.

90 J.-L. Liu and B. Eisenberg, *Physical Review E*, 2015, **92**, 012711.

91 M. Modestov, V. Bychkov, D. Valiev and M. Marklund, *The Journal of Physical Chemistry C*, 2011, **115**, 21915–21926.

92 X. Wang, B. Shapiro and E. Smela, *The Journal of Physical Chemistry C*, 2009, **113**, 382–401.

93 V. Kaphle, S. Liu, A. Al-Shadeedi, C.-M. Keum and B. Lüssem, *Advanced Materials*, 2016, **28**, 8766–8770.

94 J. T. Friedlein, J. Rivnay, D. H. Dunlap, I. McCulloch, S. E. Shaheen, R. R. McLeod and G. G. Malliaras, *Applied Physics Letters*, 2017, **111**, 023301.

95 C. Liu, Y. Xu and Y.-Y. Noh, *Materials Today*, 2015, **18**, 79–96.

96 S. S. Cohen, *Thin Solid Films*, 1983, **104**, 361–379.

97 R. L. Stoop, K. Thodkar, M. Sessolo, H. J. Bolink, C. Schönenberger and M. Calame, *Physical Review Applied*, 2017, **7**, 014009.

98 A. G. Polyravas, V. F. Curto, N. Schaefer, A. B. Calia, A. Guimera-Brunet, J. A. Garrido and G. G. Malliaras, *Flexible and Printed Electronics*, 2019, **4**, 044003.

99 K. Hong, S. Y. Yang, C. Yang, S. H. Kim, D. Choi and C. E. Park, *Organic electronics*, 2008, **9**, 864–868.

100 M. Kano, T. Minari and K. Tsukagoshi, *Applied Physics Letters*, 2009, **94**, 101.

101 M. T. Greiner, L. Chai, M. G. Helander, W.-M. Tang and Z.-H. Lu, *Advanced Functional Materials*, 2012, **22**, 4557–4568.

102 A. A. Günther, M. Sawatzki, P. Formánek, D. Kasemann and K. Leo, *Advanced Functional Materials*, 2016, **26**, 768–775.

103 A. F. Paterson, H. Faber, A. Savva, G. Nikiforidis, M. Gedda, T. C. Hidalgo, X. Chen, I. McCulloch, T. D. Anthopoulos and S. Inal, *Advanced Materials*, 2019, **31**, 1902291.

104 F. Mariani, F. Conzuelo, T. Cramer, I. Gualandi, L. Possanzini, M. Tessarolo, B. Fraboni, W. Schuhmann and E. Scavetta, *Small*, 2019, **15**, 1902534.

105 A. Savva, R. Hallani, C. Cendra, J. Surgailis, T. C. Hidalgo, S. Wustoni, R. Sheelamanthula, X. Chen, M. Kirkus, A. Giovannitti *et al.*, *Advanced Functional Materials*, 2020, **30**, 1907657.

106 H. S. White, G. P. Kittlesen and M. S. Wrighton, *Journal of the American Chemical Society*, 1984, **106**, 5375–5377.

107 M. Moser, J. F. Ponder Jr, A. Wadsworth, A. Giovannitti and I. McCulloch, *Advanced Functional Materials*, 2019, **29**, 1807033.

108 E. Zeglio and O. Inganäs, *Advanced Materials*, 2018, **30**, 1800941.

109 D. Nilsson, M. Chen, T. Kugler, T. Remonen, M. Armgarth and M. Berggren, *Advanced Materials*, 2002, **14**, 51–54.

110 S. T. Keene, T. P. van der Pol, D. Zakhidov, C. H. Weijtens, R. A. Janssen, A. Salleo and Y. van de Burgt, *Advanced Materials*, 2020, **32**, 2000270.

111 B. V. Khau, A. D. Scholz and E. Reichmanis, *Journal of Materials Chemistry C*, 2020, **8**, 15067–15078.

112 P. Jastrzebska-Perfect, G. D. Spyropoulos, C. Cea, Z. Zhao, O. J. Rauhala, A. Viswanathan, S. A. Sheth, J. N. Gelinas

and D. Khodagholy, *Science Advances*, 2020, **6**, eaaz6767.
113 D. Kim, H. Jang, S. Lee, B. J. Kim and F. S. Kim, *ACS Applied Materials & Interfaces*, 2021, **13**, 1065–1075.
114 T. Yamamoto, K. Sanechika and A. Yamamoto, *Journal of Polymer Science: Polymer Letters Edition*, 1980, **18**, 9–12.
115 C. B. Nielsen and I. McCulloch, *Progress in Polymer Science*, 2013, **38**, 2053–2069.
116 A. Marrocchi, D. Lanari, A. Facchetti and L. Vaccaro, *Energy & Environmental Science*, 2012, **5**, 8457–8474.
117 I. Osaka and R. D. McCullough, *Accounts of chemical research*, 2008, **41**, 1202–1214.
118 L. Q. Flagg, R. Giridharagopal, J. Guo and D. S. Ginger, *Chemistry of Materials*, 2018, **30**, 5380–5389.
119 L.-a. Kong, J. Sun, C. Qian, Y. Fu, J. Wang, J. Yang and Y. Gao, *Organic Electronics*, 2017, **47**, 126–132.
120 J. Nightingale, C. Pitsalidis, A.-M. Pappa, E. Tan, K. Stewart, R. Owens and J.-S. Kim, *Journal of Materials Chemistry C*, 2020, **8**, 8846–8855.
121 D. T. Duong, Y. Tuchman, P. Chakthranont, P. Cavassin, R. Colucci, T. F. Jaramillo, A. Salleo and G. C. Faria, *Advanced Electronic Materials*, 2018, **4**, 1800090.
122 C. G. Bischak, L. Q. Flagg and D. S. Ginger, *Advanced Materials*, 2020, **32**, 2002610.
123 S. Inal, J. Rivnay, P. Leleux, M. Ferro, M. Ramuz, J. C. Brendel, M. M. Schmidt, M. Thelakkat and G. G. Malliaras, *Advanced Materials*, 2014, **26**, 7450–7455.
124 J. C. Brendel, M. M. Schmidt, G. Hagen, R. Moos and M. Thelakkat, *Chemistry of Materials*, 2014, **26**, 1992–1998.
125 P. Schmode, D. Ohayon, P. M. Reichstein, A. Savva, S. Inal and M. Thelakkat, *Chemistry of Materials*, 2019, **31**, 5286–5295.
126 A. Håkansson, S. Han, S. Wang, J. Lu, S. Braun, M. Fahlman, M. Berggren, X. Crispin and S. Fabiano, *Journal of Polymer Science Part B: Polymer Physics*, 2017, **55**, 814–820.
127 J. Y. Gerasimov, R. Gabrielsson, R. Forchheimer, E. Stavrinidou, D. T. Simon, M. Berggren and S. Fabiano, *Advanced Science*, 2019, **6**, 1801339.
128 H. Yao, L. Ye, H. Zhang, S. Li, S. Zhang and J. Hou, *Chemical reviews*, 2016, **116**, 7397–7457.
129 C. B. Nielsen, A. Giovannitti, D.-T. Sbircea, E. Bandiello, M. R. Niazi, D. A. Hanifi, M. Sessolo, A. Amassian, G. G. Malliaras, J. Rivnay *et al.*, *Journal of the American Chemical Society*, 2016, **138**, 10252–10259.
130 M. Moser, L. R. Savagian, A. Savva, M. Matta, J. F. Ponder Jr, T. C. Hidalgo, D. Ohayon, R. Hallani, M. Reisjalali, A. Troisi *et al.*, *Chemistry of Materials*, 2020, **32**, 6618–6628.
131 M. Moser, T. C. Hidalgo, J. Surgailis, J. Gladisch, S. Ghosh, R. Sheelamanthula, Q. Thiburce, A. Giovannitti, A. Salleo, N. Gasparini *et al.*, *Advanced Materials*, 2020, **32**, 2002748.
132 A. Giovannitti, D.-T. Sbircea, S. Inal, C. B. Nielsen, E. Bandiello, D. A. Hanifi, M. Sessolo, G. G. Malliaras, I. McCulloch and J. Rivnay, *Proceedings of the National Academy of Sciences*, 2016, **113**, 12017–12022.
133 X. Guo and A. Facchetti, *Nature Materials*, 2020, **19**, 922–928.
134 I. McCulloch, M. Heeney, C. Bailey, K. Genevicius, I. MacDonald, M. Shkunov, D. Sparrowe, S. Tierney, R. Wagner, W. Zhang, M. L. Chabinyc, R. J. Kline, M. D. McGehee and M. F. Toney, *Nature materials*, 2006, **5**, 328–333.
135 A. Al Baroot, A. Alshammari and M. Grell, *Thin Solid Films*, 2019, **669**, 665–669.
136 A. Savva, C. Cendra, A. Giugni, B. Torre, J. Surgailis, D. Ohayon, A. Giovannitti, I. McCulloch, E. Di Fabrizio, A. Salleo, J. Rivnay and S. Inal, *Chemistry of Materials*, 2019, **31**, 927–937.
137 M. Matta, R. Wu, B. D. Paulsen, A. J. Petty, R. Sheelamanthula, I. McCulloch, G. C. Schatz and J. Rivnay, *Chemistry of Materials*, 2020, **32**, 7301–7308.
138 V. Venkatraman, J. T. Friedlein, A. Giovannitti, I. P. Maria, I. McCulloch, R. R. McLeod and J. Rivnay, *Advanced Science*, 2018, **5**, 1800453.
139 M. Li, C. An, W. Pisula and K. Mullen, *Accounts of chemical research*, 2018, **51**, 1196–1205.
140 M. Zhang, H. N. Tsao, W. Pisula, C. Yang, A. K. Mishra and K. Müllen, *Journal of the American Chemical Society*, 2007, **129**, 3472–3473.
141 H. Zhou, Y. Zhang, C.-K. Mai, S. D. Collins, T.-Q. Nguyen, G. C. Bazan and A. J. Heeger, *Advanced Materials*, 2014, **26**, 780–785.
142 C.-K. Mai, B. Russ, S. L. Fronk, N. Hu, M. B. Chan-Park, J. J. Urban, R. A. Segalman, M. L. Chabinyc and G. C. Bazan, *Energy & Environmental Science*, 2015, **8**, 2341–2346.
143 A. T. Lill, D. X. Cao, M. Schrock, J. Vollbrecht, J. Huang, T. Nguyen-Dang, V. V. Brus, B. Yurash, D. Leifert, G. C. Bazan and T.-Q. Nguyen, *Advanced Materials*, 2020, 1908120.
144 A. Giovannitti, K. J. Thorley, C. B. Nielsen, J. Li, M. J. Donahue, G. G. Malliaras, J. Rivnay and I. McCulloch, *Advanced Functional Materials*, 2018, **28**, 1706325.
145 A. Giovannitti, R. B. Rashid, Q. Thiburce, B. D. Paulsen, C. Cendra, K. Thorley, D. Moia, J. T. Mefford, D. Hanifi, D. Weiyuan, M. Moser, A. Salleo, J. Nelson, I. McCulloch and J. Rivnay, *Advanced Materials*, 2020, **32**, 1908047.
146 D. De Leeuw, M. Simenon, A. Brown and R. Einerhand, *Synthetic Metals*, 1997, **87**, 53–59.
147 X. Wu, Q. Liu, A. Surendran, S. E. Bottle, P. Sonar and W. L. Leong, *Advanced Electronic Materials*, 2021, **7**, 2170004.
148 M. Moser, A. Savva, K. Thorley, B. D. Paulsen, T. C. Hidalgo, D. Ohayon, H. Chen, A. Giovannitti, A. Marks, N. Gasparini, A. Wadsworth, J. Rivnay, S. Inal and I. McCulloch, *Angewandte Chemie International Edition*, 2020.
149 H. Sun, J. Gerasimov, M. Berggren and S. Fabiano, *Journal of Materials Chemistry C*, 2018, **6**, 11778–11784.
150 H. Sun, X. Guo and A. Facchetti, *Chem*, 2020, **6**, 1310–1326.
151 H. Jia and T. Lei, *Journal of Materials Chemistry C*, 2019, **7**, 12809–12821.
152 A. Giovannitti, C. B. Nielsen, D.-T. Sbircea, S. Inal, M. Donahue, M. R. Niazi, D. A. Hanifi, A. Amassian, G. G. Malliaras, J. Rivnay and I. McCulloch, *Nature communications*, 2016,

7, 13066.

153 A. Giovannitti, I. P. Maria, D. Hanifi, M. J. Donahue, D. Bryant, K. J. Barth, B. E. Makdah, A. Savva, D. Moia, M. Zetek, P. R. Barnes, O. G. Reid, S. Inal, G. Rumbles, G. G. Malliaras, J. Nelson, J. Rivnay and I. McCulloch, *Chemistry of Materials*, 2018, **30**, 2945–2953.

154 A. F. Paterson, A. Savva, S. Wustoni, L. Tsetseris, B. D. Paulsen, H. Faber, A. H. Emwas, X. Chen, G. Nikiforidis, T. C. Hidalgo, M. Moser, I. P. Maria, J. Rivnay, I. McCulloch, T. D. Anthopoulos and S. Inal, *Nature Communications*, 2020, **11**, 3004.

155 A. Savva, D. Ohayon, J. Surgailis, A. F. Paterson, T. C. Hidalgo, X. Chen, I. P. Maria, B. D. Paulsen, A. J. Petty, J. Rivnay, I. McCulloch and S. Inal, *Advanced Electronic Materials*, 2019, **5**, 1900249.

156 M. Kawan, T. C. Hidalgo, W. Du, A.-M. Pappa, R. Owens, I. McCulloch and S. Inal, *Materials Horizons*, 2020, **7**, 2348–2358.

157 Z. Chen, Y. Zheng, H. Yan and A. Facchetti, *Journal of the American Chemical Society*, 2009, **131**, 8–9.

158 D. Ohayon, G. Nikiforidis, A. Savva, A. Giugni, S. Wustoni, T. Palanisamy, X. Chen, I. P. Maria, E. Di Fabrizio, P. M. F. J. Costa, I. McCulloch and S. Inal, *Nature materials*, 2020, **19**, 456–463.

159 A. M. Pappa, D. Ohayon, A. Giovannitti, I. P. Maria, A. Savva, I. Uguz, J. Rivnay, I. McCulloch, R. M. Owens and S. Inal, *Science advances*, 2018, **4**, eaat0911.

160 H. Sun, M. Vagin, S. Wang, X. Crispin, R. Forchheimer, M. Berggren and S. Fabiano, *Advanced Materials*, 2018, **30**, 1704916.

161 X. Chen, A. Marks, B. D. Paulsen, R. Wu, R. B. Rashid, H. Chen, M. Alsufyani, J. Rivnay and I. McCulloch, *Angewandte Chemie International Edition*, 2020.

162 J. Mei and Z. Bao, *Chemistry of Materials*, 2014, **26**, 604–615.

163 Y. Wang, E. Zeglio, H. Liao, J. Xu, F. Liu, Z. Li, I. P. Maria, D. Mawad, A. Herland, I. McCulloch *et al.*, *Chemistry of Materials*, 2019, **31**, 9797–9806.

164 L. Q. Flagg, C. G. Bischak, J. W. Onorato, R. B. Rashid, C. K. Luscombe and D. S. Ginger, *Journal of the American Chemical Society*, 2019, **141**, 4345–4354.

165 P. Schmode, A. Savva, R. Kahl, D. Ohayon, F. Meichsner, O. Dolynchuk, T. Thurn-Albrecht, S. Inal and M. Thelakkat, *ACS Applied Materials & Interfaces*, 2020, **12**, 13029–13039.

166 D. Moia, A. Giovannitti, A. A. Szumska, I. P. Maria, E. Rezasoltani, M. Sachs, M. Schnurr, P. R. Barnes, I. McCulloch and J. Nelson, *Energy & Environmental Science*, 2019, **12**, 1349–1357.

167 I. P. Maria, B. D. Paulsen, A. Savva, D. Ohayon, R. Wu, R. Hallani, A. Basu, W. Du, T. D. Anthopoulos, S. Inal *et al.*, *Advanced Functional Materials*, 2021, 2008718.

168 D. Ohayon, A. Savva, W. Du, B. D. Paulsen, I. Uguz, R. S. Ashraf, J. Rivnay, I. McCulloch and S. Inal, *ACS Applied Materials & Interfaces*, 2021, **13**, 4253–4266.

169 M. J. Dyson, E. Lariou, J. Martin, R. Li, H. Erothu, G. Wantz, P. D. Topham, O. J. Dautel, S. C. Hayes, P. N. Stavrinou *et al.*, *Chemistry of Materials*, 2019, **31**, 6540–6547.

170 C. M. Pacheco-Moreno, M. Schreck, A. D. Scaccabarozzi, P. Bourgun, G. Wantz, M. M. Stevens, O. J. Dautel and N. Stingelin, *Advanced Materials*, 2017, **29**, 1604446.

171 T. Nicolini, J. Surgailis, A. Savva, A. D. Scaccabarozzi, R. Nakar, D. Thuau, G. Wantz, L. J. Richter, O. Dautel, G. Hadziioannou *et al.*, *Advanced Materials*, 2021, **33**, 2005723.

172 L. R. Savagian, A. M. Österholm, J. F. Ponder Jr, K. J. Barth, J. Rivnay and J. R. Reynolds, *Advanced Materials*, 2018, **30**, 1804647.

173 Z. S. Parr, R. Halaksa, P. A. Finn, R. B. Rashid, A. Kovalenko, M. Weiter, J. Rivnay, J. Krajcovic and C. B. Nielsen, *ChemPlusChem*, 2019, **84**, 1384–1390.

174 A. K. Williams, J. Tropp, E. R. Crater, N. Eedugurala and J. D. Azoulay, *ACS Applied Polymer Materials*, 2019, **1**, 309–314.

175 W. Hai, T. Goda, H. Takeuchi, S. Yamaoka, Y. Horiguchi, A. Matsumoto and Y. Miyahara, *Sensors and Actuators B: Chemical*, 2018, **260**, 635–641.

176 C. G. Bischak, L. Q. Flagg, K. Yan, T. Rehman, D. W. Davies, R. J. Quezada, J. W. Onorato, C. K. Luscombe, Y. Diao, C.-Z. Li *et al.*, *Journal of the American Chemical Society*, 2020, **142**, 7434–7442.

177 S. Ghosh and I. Zozoulenko, *ACS Applied Electronic Materials*, 2020.

178 S. Zokaei, R. Kroon, J. Gladisch, B. D. Paulsen, W. Sohn, A. I. Hofmann, G. Persson, A. Stamm, P.-O. Syrén, E. Olsson *et al.*, *Advanced Science*, 2021, **8**, 2002778.

179 Kenry and B. Liu, *Biomacromolecules*, 2018, **19**, 1783–1803.

180 H. Tran, V. R. Feig, K. Liu, H.-C. Wu, R. Chen, J. Xu, K. Deisseroth and Z. Bao, *ACS central science*, 2019, **5**, 1884–1891.

181 D. Vanmaekelbergh, A. Houtepen and J. Kelly, *Electrochimica Acta*, 2007, **53**, 1140–1149.

182 D. A. Bernards, D. J. Macaya, M. Nikolou, J. A. DeFranco, S. Takamatsu and G. G. Malliaras, *Journal of Materials Chemistry*, 2008, **18**, 116–120.

183 A. J. Bard and L. R. Faulkner, *Electrochemical Methods Fundamentals and Applications*, John Wiley & Sons, 2nd edn, 2001.

184 V. S. Bagotsky, *Fundamentals of electrochemistry*, John Wiley & Sons, 2005, vol. 44.

185 H. Tang, P. Kumar, S. Zhang, Z. Yi, G. D. Crescenzo, C. Santato, F. Soavi and F. Cicoira, *ACS applied materials & interfaces*, 2015, **7**, 969–973.

186 G. Tarabella, C. Santato, S. Y. Yang, S. Iannotta, G. G. Malliaras and F. Cicoira, *Applied Physics Letters*, 2010, **97**, 205.

187 C. Liao, M. Zhang, L. Niu, Z. Zheng and F. Yan, *Journal of Materials Chemistry B*, 2013, **1**, 3820–3829.

188 X. Xi, D. Wu, W. Ji, S. Zhang, W. Tang, Y. Su, X. Guo and R. Liu, *Advanced Functional Materials*, 2020, **30**, 1905361.

189 P. Andersson, R. Forchheimer, P. Tehrani and M. Berggren, *Advanced Functional Materials*, 2007, **17**, 3074–3082.

190 I. Gualandi, M. Marzocchi, E. Scavetta, M. Calienni, A. Bonfiglio and B. Fraboni, *Journal of Materials Chemistry B*, 2015, **3**, 6753–6762.

191 F. Mariani, I. Gualandi, M. Tessarolo, B. Fraboni and E. Scavetta, *ACS applied materials & interfaces*, 2018, **10**, 22474–22484.

192 F. Cicoira, M. Sessolo, O. Yaghmazadeh, J. A. DeFranco, S. Y. Yang and G. G. Malliaras, *Advanced Materials*, 2010, **22**, 1012–1016.

193 P. C. Hütter, T. Rothländer, A. Haase, G. Trimmel and B. Stadlober, *Applied Physics Letters*, 2013, **103**, 043308.

194 M. Kettner, I. Vladimirov, A. J. Strudwick, M. G. Schwab and R. T. Weitz, *Journal of Applied Physics*, 2015, **118**, 025501.

195 S. T. Koshy, R. M. Desai, P. Joly, J. Li, R. K. Bagrodia, S. A. Lewin, N. S. Joshi and D. J. Mooney, *Advanced healthcare materials*, 2016, **5**, 541–547.

196 Y. Dong, M. Rodrigues, X. Li, S. H. Kwon, N. Kosaric, S. Khong, Y. Gao, W. Wang and G. C. Gurtner, *Advanced Functional Materials*, 2017, **27**, 1606619.

197 Y. J. Jo, K. Y. Kwon, Z. U. Khan, X. Crispin and T.-i. Kim, *ACS applied materials & interfaces*, 2018, **10**, 39083–39090.

198 C. P. H. Rajapaksha, C. Feng, C. Piedrahita, J. Cao, V. Kaphle, B. Lüssem, T. Kyu and A. Jákli, *Macromolecular Rapid Communications*, 2020, **41**, 1900636.

199 C. Feng, C. Rajapaksha, C. Piedrahita, J. Cao, A. Jakli and T. Kyu, *APS*, 2019, **2019**, E50–010.

200 S. Chen, A. Surendran, X. Wu and W. L. Leong, *Advanced Functional Materials*, 2020, **30**, 2006186.

201 L. J. Currano, F. C. Sage, M. Hagedon, L. Hamilton, J. Patrone and K. Gerasopoulos, *Scientific Reports*, 2018, **8**, 15890.

202 D. Khodagholy, J. N. Gelinas, T. Thesen, W. Doyle, O. Devinsky, G. G. Malliaras and G. Buzsáki, *Nature neuroscience*, 2015, **18**, 310–315.

203 S. Pecqueur, D. Guérin, D. Vuillaume and F. Alibart, *Organic Electronics*, 2018, **57**, 232–238.

204 P. Kumar, Z. Yi, S. Zhang, A. Sekar, F. Soavi and F. Cicoira, *Applied Physics Letters*, 2015, **107**, 053303.

205 J. Rivnay, S. Inal, B. A. Collins, M. Sessolo, E. Stavrinidou, X. Strakosas, C. Tassone, D. M. Delongchamp and G. G. Malliaras, *Nature communications*, 2016, **7**, 11287.

206 P. A. Ersman, D. Nilsson, J. Kawahara, G. Gustafsson and M. Berggren, *Organic electronics*, 2013, **14**, 1276–1280.

207 E. Bihar, Y. Deng, T. Miyake, M. Saadaoui, G. G. Malliaras and M. Rolandi, *Scientific reports*, 2016, **6**, 1–6.